JOURNAL OF MATERIALS SCIENCE **38** (2003) 4639–4660

Ceramic electrolytes and electrochemical sensors

C. O. PARK
Department of Materials Science and Engineering, KAIST, Taejon 305-701, Korea
E-mail: cops@kaist.ac.kr

S. A. AKBAR
Department of Materials Science and Engineering, CISM, 291 Watts Hall, Ohio State University, Columbus, OH 43210, USA

W. WEPPNER
Christian-Albrechts University of Kiel, Kaiserstrasse 2, D-24143, Kiel, Germany

The electrochemical method involving solid electrolytes has been known as a selective and an accurate way of sensing chemical species in the environment and even in liquid metal for some time. The most successful among the electrochemical sensors are the emission control sensor (λ-sensor) for the automobile engine and the oxygen sensor used in steelmaking, both made of stabilized zirconia. This article presents an overview of basic principles of various types of electrochemical sensors including active (potentiometric) and passive (amperometric) sensors. Recent advances in oxygen (O_2), carbon dioxide (CO_2) and hydrogen (H_2) sensors are also presented.

1. Introduction

The solid-state electrochemical method has been known as a selective and an accurate way of sensing chemical species in the environment and even in the liquid metal for some time. After the first interpretation of the ion-conduction mechanism in zirconia [1] by Carl Wagner in 1943, there have been substantial advances in the development of solid ionic materials that are extensively being used in electrochemical sensors. The most successful among these sensors is the emission control sensor made of stabilized zirconia for the automobile engine. It made a revolutionary change in the automobile engine from the use of caburator to the electronic fuel injection.

In this paper, we review basic principles of various types of electrochemical sensors including active (potentiometric) and passive (amperometric)) sensors. Recent advances in oxygen, CO_2 and hydrogen sensors are also being presented.

2. Solid electrolytes

Solid electrolytes exhibit dominant ionic conductivity resulting from the migration of ions through point defect sites in the lattice. The defects are created either by thermal activation with E_a ranging from 0.7 to 1.4 eV, or by compensation of aliovalent dopants. Compared to the conductivities of insulating ceramics with $\sigma \leq 10^{-10}$ Scm^{-1}, the conductivities of solid electrolytes generally are $\sigma \geq 10^{-5}$ Scm^{-1} with an ionic transference number (t_{ion}) greater than 0.99. The Hittorf transference number t_i is defined as the fraction of charge carried by species i, which, upon passage of current, migrates toward the cathode or anode, depending on the polarity of the ions. In terms of partial conductivities,

$$t_i = \sigma_i \Big/ \sum_k \sigma_k \tag{1}$$

and its sum for all the current-carrying species must be unity in a given material.

$$\sum_i t_i = 1 \tag{2}$$

The molar transference number [2], t_i^* is defined as the fractional moles of species, i, which migrates toward the cathode upon passing current. If anionic species j migrate toward the anode, t_j^* becomes a negative value. Therefore, the molar transference number, t_i^* is related to the Hittorf transference number, t_i by

$$t_i^* = t_i / z_i \tag{3}$$

The total conductivity σ_T becomes the sum of all the contributions from the mobile species in the electrolyte expressed as

$$\sigma_T = \sum_i \mu_i q_i c_i \tag{4}$$

where μ_i, q_i and c_i correspond to the electrochemical mobility, the amount of charge per carrier, and the concentration of mobile species i contributing to the current flow, respectively. If the mobility is independent of concentration, the concentration of charge carriers in the electrolyte plays an important role in determining the relative conductivity contribution.

In solid electrolytes comprising of a pure binary compound, MX, ionic defect species would be

thermally produced mainly through Schottky-Wagner (Equation 5), Frenkel (Equation 6) or anti-Frenkel (Equation 7) equilibria written as

$$\mathrm{O} = V_{\mathrm{M}}'' + V_{\mathrm{X}}^{\bullet\bullet} \quad K_{\mathrm{S}} = [V_{\mathrm{M}}''][V_{\mathrm{X}}^{\bullet\bullet}] \tag{5}$$

$$\mathrm{O} = V_{\mathrm{M}}'' + M_{\mathrm{i}}^{\bullet\bullet} \quad K_{\mathrm{F}} = [V_{\mathrm{M}}''][M_{\mathrm{i}}^{\bullet\bullet}] \tag{6}$$

$$\mathrm{O} = V_{\mathrm{X}}^{\bullet\bullet} + X_{\mathrm{i}}'' \quad K_{\mathrm{AF}} = [V_{\mathrm{X}}^{\bullet\bullet}][X_{\mathrm{i}}''] \tag{7}$$

where K_{S}, K_{F} and K_{AF} are the mass action constants for Schottky-Wagner, Frenkel and anti-Frenkel defects, respectively. In addition, the electronic defects would be produced through the electron-hole recombination reaction.

$$\mathrm{O} = e' + h^{\bullet} \quad K_{\mathrm{i}} = [e'][h^{\bullet}] \tag{8}$$

These defects would satisfy the electro-neutrality condition (ENC) generally expressed as in Equation 9, equating the total positive charge to the total negative charge.

$$\sum_i z_{\mathrm{i}}[\oplus^{z+}] = \sum_j z_{\mathrm{j}}[\ominus^{z-}] \tag{9}$$

For instance, the ENC for electrolytes with Frenkel defects can be written as $2[M_{\mathrm{i}}^{\bullet\bullet}] + [h^{\bullet}] = 2[V_{\mathrm{M}}''] + [e']$. The formation or annihilation of $[M_{\mathrm{i}}^{\bullet\bullet}]$ or $[V_{\mathrm{M}}'']$ is controlled via reversible interaction of the electrolyte with the surrounding. In conjunction with the ENC and Equation 6, the concentration of each defect can be obtained as a function of the chemical activity of the metal or the conjugate non-metal component in the electrolyte (see the Kroger-Vink diagram of Fig. 1a). Knowing the defect mobilities, the partial conductivity for each species can also be determined using Equation 4, as seen in Fig. 1b.

Since the mobilities of electrons and holes are much higher (more than 1000 times) than those of ions, the concentration of ionic defects has to exceed those of electrons and holes by many orders of magnitude in order to behave as a solid electrolyte. There are two ways of satisfying the criterion for a solid electrolyte. First, according to the Kroger-Vink diagram for Frenkel defects in a pure compound MX shown in Fig. 1a, dominant ionic conductivity can only be achieved when the stoichiometric binary compound exhibits a relatively high value of K_{F} compared to K_{i}.

In the near-stoichiometry region where the concentration of ionic defects is many orders of magnitude higher than that of electrons or holes, the ionic conductivity becomes dominant over the electronic conductivity ($t_{\mathrm{ion}} > 0.99$). This is referred to as an electrolytic domain for solid electrolytes such as AgCl and AgBr. For t_{ion} between 0.01 and 0.99, the mixed conduction is considered to occur.

Secondly, when the concentrations of ionic defects for a pure compound are insufficient for dominant ionic conduction, the ionic conductivity can be raised by doping the compound with aliovalent impurities. As a specific example, pure ZrO_2 does not have large enough oxygen ion defect concentration to exhibit dominant ionic conduction. But the substitution of soluble dopant ions such as Mg^{2+}, Ca^{2+} or Y^{3+} on Zr^{4+} lattice sites,

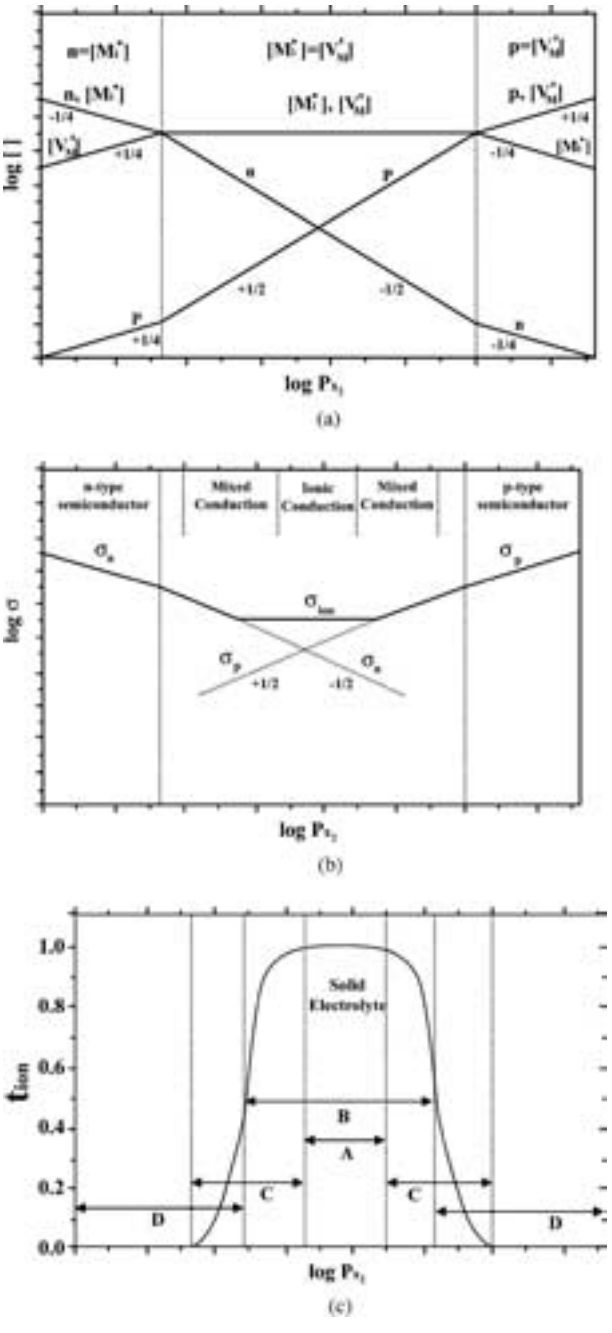

Figure 1 (a) Kroger-Vink diagram for a pure solid electrolyte with Frenkel-type defects, (b) the total conductivity vs. log P_{X_2}, and (c) the ionic transference number vs. log P_{X_2} [3]. A: electrolytic conduction domain ($t_{\mathrm{ion}} > 0.99$) B: ionic conduction domain ($t_{\mathrm{ion}} > 0.5$) C: mixed conduction domain ($0.01 < t_{\mathrm{ion}} < 0.99$) D: electronic conduction domain ($t_{\mathrm{ion}} < 0.5$).

where these dopants having lower valences than Zr host ions, act as electron acceptors. The ENC condition for an acceptor ion with a valence of 2+ such as Ca^{2+} becomes

$$[\mathrm{O}_{\mathrm{i}}''] + 2[\mathrm{Ca}_{\mathrm{Zr}}''] + [e'] = 2[V_{\mathrm{O}}^{\bullet\bullet}] + [h^{\bullet}] \tag{10}$$

where $[\mathrm{O}_{\mathrm{i}}'']$ is negligibly small. For intentionally doped crystals, $[\mathrm{Ca}_{\mathrm{Zr}}'']$ dominates on the left-hand side of Equation 10 and electrical neutrality is achieved either through $2[\mathrm{Ca}_{\mathrm{Zr}}''] \cong [h^{\bullet}]$ or $[\mathrm{Ca}_{\mathrm{Zr}}''] \cong [V_{\mathrm{O}}^{\bullet\bullet}]$, depending on the oxygen partial pressure in the ambient. In the near-stoichiometry region, where doped ZrO_2 is mostly used, ionic compensation is dominant whereas

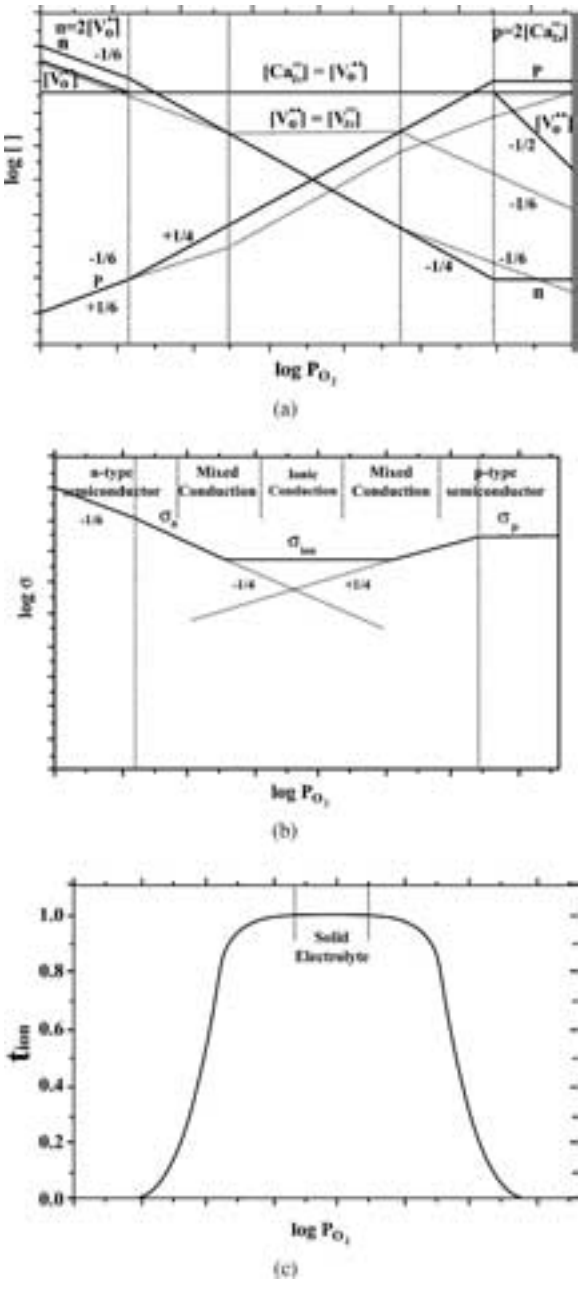

Figure 2 (a) Kroger-Vink diagram for intrinsic ZrO_2 (dotted line) and CaO-doped ZrO_2 (solid line) (b) the total conductivity for CaO-doped ZrO_2 vs. P_{O_2} (c) transference number of ions vs. log P_{O_2} [4].

electronic compensation only becomes important at high oxygen pressure in the p-type electronic conduction domain, or else at very low oxygen pressure where n-type electronic conduction occurs. Upon neglecting the association of $[Ca''_{Zr}]$ and $[V_O^{\bullet\bullet}]$, the dependence of the concentrations of mobile charged species on oxygen partial pressure is shown in Fig. 2 [4].

The group IV-B refractory oxides of ZrO_2, HfO_2, CeO_2 and ThO_2 are oxygen ion conductors having the cubic fluorite structure. While ThO_2 and CeO_2 are stable in the fluorite structure as pure compounds; the fluorite structure for pure ZrO_2 is only stable above 2300°C. But the addition of CaO or Y_2O_3 to ZrO_2 stabilizes the fluorite structure at a much lower temperature, leading to the so-called "stabilized zirconia." Generally, about 5 to 15 mol% of the dopant elements are added for stabilization. The electrical properties of some of the principal oxygen ion conductors are compared in Table I.

TABLE I Electrical properties of oxide ion conducting solid electrolytes

Electrolyte	Ionic conductivity at 1000°C ($\Omega^{-1}cm^{-1}$)	Activation energy (eV)
ZrO_2 + 12 mol% CaO	0.055	1.1
ZrO_2 + 9 mol% Y_2O_3	0.12	0.8
ThO_2 + 8 mol% Y_2O_3	0.0048	1.1
ThO_2 + 5 mol% CaO	0.00047	1.1
CeO_2 + 11 mol% La_2O_3	0.08	0.91
CeO_2 + 15 mol% CaO	0.025	0.75
HfO_2 + 8 mol% Y_2O_3	0.029	1.1
HfO_2 + 12 mol% CaO	0.004	1.4

For the solid electrolytes illustrated in Figs 1 and 2, the ionic conductivity is virtually independent of $P_{O_2}(P_{X_2})$. In contrast, their excess electron and hole conductivities, σ_n and σ_p are found to be proportional to $P_{X_2}^{-1/n}$ and $P_{X_2}^{+1/n}$, respectively, where n is independent of P_{X_2} and T, and is determined by the defect formation reaction for the solid electrolyte. However, all three conductivity modes exhibit an Arrhenius-type temperature dependence with apparent activation energies, Q_{ion}, Q_n and Q_p which are also independent of P_{X_2} and T. As a result,

$$\sigma_{ion} = \sigma^{\circ}_{ion} \exp\left(-\frac{Q_{ion}}{RT}\right) \tag{11}$$

$$\sigma_n = \sigma^{\circ}_n P_{X_2}^{-1/n} \exp\left(-\frac{Q_{\ominus}}{RT}\right) \tag{12}$$

$$\sigma_p = \sigma^{\circ}_p P_{X_2}^{1/n} \exp\left(-\frac{Q_{\oplus}}{RT}\right) \tag{13}$$

where the quantities Q_{ion}, $Q_{\ominus}$, $Q_{\oplus}$, n, σ°_{ion}, σ°_n and σ°_p are all constants independent of P_{X_2} and T. The total conductivity, σ_T then becomes

$$\sigma_T = \sigma_{ion} + \sigma_n + \sigma_p \tag{14}$$

Accordingly, a three-dimensional Patterson conductivity diagram can be constructed, as in Fig. 3, for the corresponding $\log \sigma$ surface of ionic, electronic and hole conductivities as a function of $\log P_{X_2}$ and $1/T$.

In Fig. 3, domains exist wherein only one conduction behavior (ionic, electron or hole) individually dominates over the others. In region A, σ_p is greater than

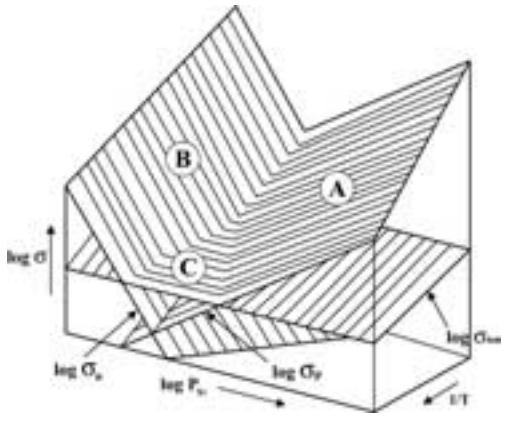

Figure 3 Patterson plot of $\log \sigma$ as a function of $\log P_{X_2}$ and $1/T$ [5].

either σ_{ion} or σ_n so that $\log \sigma_T$ and $\log \sigma_p$ are virtually identical. In region B, the $\log \sigma_T$ surface conforms to the $\log \sigma_n$ plane whereas the $\log \sigma_{ion}$ plane dominates in region C. The projections of these regions onto the $\log P_{X_2}$ and $1/T$ plane provide the map for hole, electron and electrolytic conduction domains for the solid electrolyte [5].

The dominant domain can be found by equating the appropriate conductivity equations and then rearranging terms. For example, the σ_p to σ_n transition boundary can be calculated as the locus of $\log P_{X_2}$ and $1/T$ points where $\sigma_p = \sigma_n$. This leads to

$$\log P_{X_2}(\sigma_p = \sigma_n) = -\frac{n}{2}\left(\frac{Q_\ominus - Q_\oplus}{2.303R}\right)\frac{1}{T} + \frac{n}{2}\log\frac{\sigma_n^\circ}{\sigma_p^\circ} \tag{15}$$

This locus of $\log P_{X_2}$ and $1/T$ points plots as a straight line with slope $-n/2[(Q_\ominus - Q_\oplus)/2.303R]$ and intercept $n/2\log(\sigma_n^\circ/\sigma_p^\circ)$. Similarly, the ionic domain boundaries can be deduced by equating individually σ_p and σ_n to σ_{ion} which gives

$$\log P_{X_2}(\sigma_p = \sigma_{ion}) = -n\left(\frac{Q_{ion} - Q_\oplus}{2.303R}\right)\frac{1}{T} + n\log\frac{\sigma_{ion}^\circ}{\sigma_p^\circ} \tag{16}$$

$$\log P_{X_2}(\sigma_n = \sigma_{ion}) = n\left(\frac{Q_{ion} - Q_\ominus}{2.303R}\right)\frac{1}{T} - n\log\frac{\sigma_{ion}^\circ}{\sigma_n^\circ} \tag{17}$$

Fig. 4 shows the relationships among the various domain boundaries corresponding to cationic and anionic conducting electrolytes. Ionic conduction prevails at lower temperature over a given range of P_{X_2} whereas electronic conduction occurs at high temperature, where the thermal generation of electronic defects becomes more important.

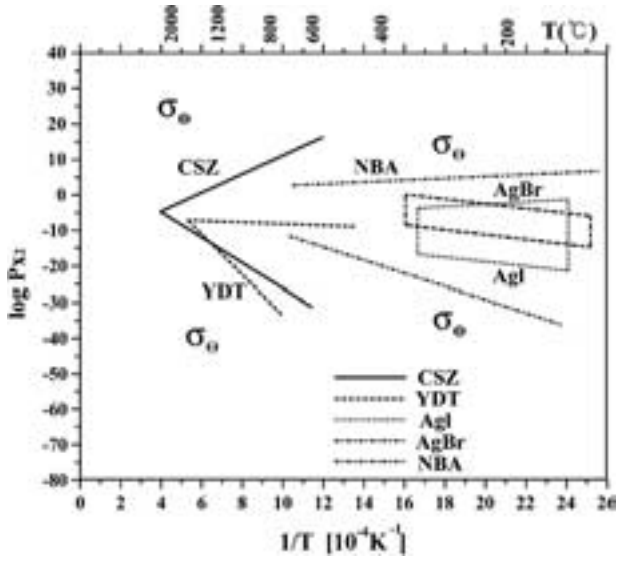

Figure 4 Map for domain boundaries of ionic, electronic, and hole conduction in $\log P_{X_2}(a_M)$ and $1/T$ [5, 6]. CSZ: Calcia-Stabilized Zirconia, YDT: Yttria Doped Thoria, NBA: Na-β-Alumina.

3. Electrodes

The electrode in a solid-state cell, which is an electronic conductor, converts the thermodynamic Galvanic potential developed in the electrolyte or at the interface into an electrical potential which is measurable experimentally. For a local electrochemical reaction (18) occurring at an electrode in contact with a solid electrolyte where M^+ is the mobile species,

$$M^+ + e' = M \tag{18}$$

the changes in the chemical potential of M are realized as changes in the electrochemical potential of electrons in the electrode, i.e., changes in the Galvanic potential of the electrode, because the electrochemical potential of M^+ ions in the electrolyte is practically constant due to its high concentration and mobility. Depending on the reversibility of reaction (18), electrodes can be classified as polarizable and non-polarizable. Wagner [7] has discussed various types of electrodes and their possible combinations to form solid electrolyte galvanic cells.

3.1. Ideally non-polarizable electrodes

At non-polarizable electrodes, the electrochemical reaction (18) occurs reversibly so that the equilibrium state is maintained among mobile ions, electrons and neutral species for the passage of small currents imposed on the cell. Therefore, these are referred to as reversible electrodes. They are generally characterized as completely leaky or non-blocking, where the charged species arriving (or leaving) at the electrode/electrolyte interface can easily cross the interface. In an electrical analogy, this corresponds to a pure resistor with zero resistance. Since the local equilibrium is maintained, reversible electrodes have a uniform electrochemical potential for each species across the electrode/electrolyte interface, which can be interpreted to provide thermodynamic information.

In practice, non-polarizable electrodes, depending on whether the electrode materials are involved in the electrochemical reactions or not, can be considered as active or inert. For example, in the cell (19) where both Ag^+ and Br^- ions contribute to the conductivity of AgBr, the Ag electrode is an active reversible electrode with respect to the Ag^+ ion, while the graphite electrode is an inert reversible electrode with respect to the Br^- ion and Br_2 gas in the ambient [7].

$$\text{Ag} \,|\text{AgBr}|\, \text{Graphite}, \text{Br}_2 \tag{19}$$

3.2. Ideally polarizable (blocking) electrodes

The electrochemical reaction (18) occurring at a polarizable electrode cannot be held in an equilibrium state, nor is the electrode reaction reversible. The information obtained from the electrode does not correspond to any well defined thermodynamic state. For such a non-reversible electrode, upon passage of a small current through the cell, the charged species in the electrolyte cannot reversibly cross the interface with this

blocking electrode. Then an interfacial over-potential is generated, resulting from a discontinuity or gradient in activity for the mobile species across the electrode/electrolyte interface. In electrical analogy, this response is the same as that of a pure capacitor. For example, for the passage of the current in the cell (19), the Ag electrode is non-reversible with respect to supplying the Br^- ion and the graphite electrode is blocking to the reduction of the Ag^+ ion.

3.3. Electrodes for electrochemical sensors

Any real electrode usually shows an intermediate property between an ideally non-polarizable and an ideally polarizable electrode whereby a fraction of the mobile species can cross the interface. In equivalent circuit analogy, this corresponds to a capacitor connected in parallel with a resistor. The ideally non-polarizable and ideally polarizable electrodes simply correspond to the extreme cases of zero resistance and infinite resistance, respectively, as illustrated in Fig. 5.

In an electrochemical sensor comprising of a reference electrode and a working electrode, non-polarizable reference electrodes are preferred because of their well defined thermodynamic state. The reversible reference electrode must have a fixed and known potential independent of the ambient, while the sensing electrode must quickly equilibrate with the ambient to form a reversible electrode. The polarizability of the electrode can be tested from the current-voltage response as shown schematically in Fig. 6. The polarizable electrode in Fig. 6a produces a large over-potential for a small amount of current passage, whereas the non-polarizable electrode in Fig. 6b can accommodate high current with little change in potential.

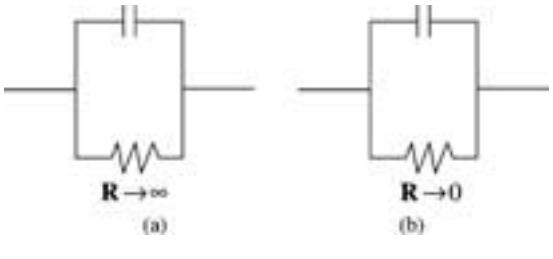

Figure 5 Equivalent circuits of (a) ideally polarizable electrode and (b) ideally non-polarizable electrode.

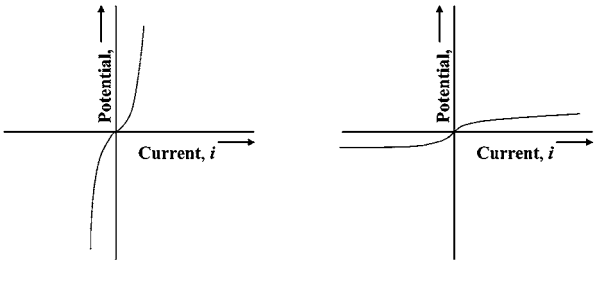

Figure 6 Current-Voltage responses of (a) highly polarizable and (b) highly non-polarizable electrodes.

4. Electromotive force of a Galvanic cell

The voltage of the Galvanic cell in Fig. 7, measured between electronic conducting electrodes A (negative) and B (positive), which are reversible with respect to mobile M^{z_M+} ions, is proportional to the electrochemical potential difference of electrons measured by the two Cu lead wires in a voltage-measuring instrument. For example, the electrical balancing voltage imposed by an external potentiometer prevents the mobile ions from moving through the internal Galvanic cell. Thus the voltage, E (often called emf) can be expressed as

$$E = -\left(\tilde{\mu}_e^{Cu2} - \tilde{\mu}_e^{Cu1}\right)/F \tag{20}$$

where $\tilde{\mu}_e \equiv \mu_e - F\Phi$, the molar electrochemical potential of electrons $\tilde{\mu}_e$, is the sum of molar chemical potential of the electrons μ_e, and the Galvanic potential energy of a mole of electrons, $-F\Phi$. The Galvanic potential is defined as the work done on the system when unit positive charge is moved from infinity to the location of interest. Here it is implicitly assumed that the solid electrolyte is homogeneous in composition i.e., no chemical work occurs in the movement of positive ions. Since wires of the same metal are generally used for the measurement of the voltage as electron probes, the chemical potential of electrons, μ_e is equal for the lead wires Cu1 and Cu2. Thus, Equation 20 simply becomes

$$E = \Phi^{Cu2} - \Phi^{Cu1} \tag{21}$$

Therefore, the voltage measured between probe Cu1 and Cu2 becomes the Galvanic potential difference that exists across the ionic conductor. In the case of an electron conductor such as a p/n diode, a Galvanic potential difference of about 0.7 V arises at the junction due to a large change in electron and hole concentrations across the interface. However, the measured voltage is always zero because the electrochemical potentials of electrons are equal for both p-type and n-type Si.

The total Galvanic potential difference in Equation 21 can be divided into two parts for the Galvanic cell in Fig. 7: ① a potential profile (junction potential) built in the electrolyte due to any inhomogeneous distribution of mobile ions, and ② two interface potentials at the electrode/electrolyte interfaces.

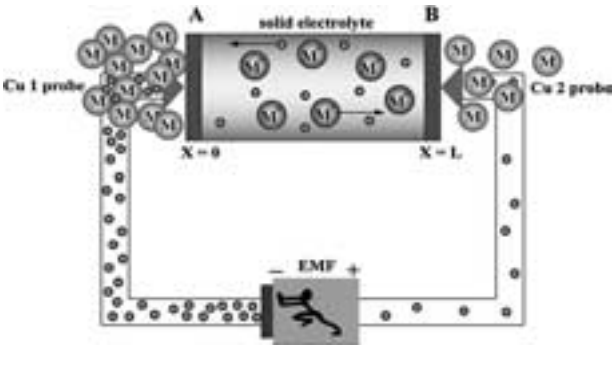

Figure 7 Galvanic cell comprising of electrodes A and B with a solid electrolyte in between.

The junction potential is a general phenomenon that occurs because of a spatial distribution in the concentrations of charged species having different mobilities. It can be easily evaluated from the general phenomenological transport equations for a multi-component conduction process where the charged species in the electrolyte are driven by gradients in the electrochemical potentials of the corresponding ions [8]. The ionic current density can be expressed as

$$J_{\mathrm{i}}(x) = -\frac{\sigma_{\mathrm{i}}(x)}{z_{\mathrm{i}}F}\left(\frac{\mathrm{d}\tilde{\mu}_{\mathrm{i}}(x)}{\mathrm{d}x}\right) \tag{22}$$

where the electrochemical potential of the ion i is again defined as

$$\tilde{\mu}_{\mathrm{i}}(x) = \mu_{\mathrm{i}}(x) + z_{\mathrm{i}}F\Phi(x) \tag{23}$$

and σ_{i} corresponds to the conductivity of ion i in the electrolyte. Combining Equations 22 and 23, the Galvanic potential gradient can be expressed as

$$\frac{\mathrm{d}\Phi(x)}{\mathrm{d}x} = -\frac{J_{\mathrm{i}}(x)}{\sigma_{\mathrm{i}}(x)} - \frac{1}{z_{\mathrm{i}}F}\left(\frac{\mathrm{d}\mu_{\mathrm{i}}(x)}{\mathrm{d}x}\right) \tag{24}$$

Since the partial current, $J_{\mathrm{i}}(x)$ at a given location in the electrolyte cannot be measured, the total current that maintains a constant value throughout the electrolyte has to be taken into account in Equation 24. This can be achieved by multiplying σ_{i} on both sides of Equation 24 and summing over all the charge carriers, which gives

$$\frac{\mathrm{d}\Phi(x)}{\mathrm{d}x}\sum_i \sigma_{\mathrm{i}} = -\left[J + \sum_i \frac{\sigma_{\mathrm{i}}}{z_{\mathrm{i}}F}\left(\frac{\mathrm{d}\mu_{\mathrm{i}}}{\mathrm{d}x}\right)\right] \tag{25}$$

where $\sum_i \sigma_{\mathrm{i}}$ corresponds to the total conductivity of the electrolyte at location x, $\sigma_{\mathrm{T}}(x)$. Integration of Equation 25 from $x = 0$ (electrode A) to $x = L$ (electrode B) gives the Galvanic potential difference of the cell (7) expressed as

$$\begin{aligned} E &= \Phi(L) - \Phi(0) \\ &= -\int_0^L \left(\frac{J}{\sigma_{\mathrm{T}}} + \sum_i \frac{t_{\mathrm{i}}}{z_{\mathrm{i}}F}\frac{\mathrm{d}\mu_{\mathrm{i}}}{\mathrm{d}x}\right)\mathrm{d}x \end{aligned} \tag{26}$$

Equation 26 is the general current-voltage relationship for a multi-component conduction system. The first term in the integral does not result from the thermodynamic properties of the cell, but accounts for the IR drop in the electrolyte. However, when the open-circuit voltage of the cell is measured, the current imposed to the circuit by an electrometer or other high-impedance voltage-measuring device is negligible. In this case, Equation 26 becomes the open-circuit potential, which was derived by Wagner [9] and others [8, 10, 11] and is expressed as

$$\Phi(L) - \Phi(0) = -\frac{1}{F}\sum_i \int_0^L \frac{t_{\mathrm{i}}}{z_{\mathrm{i}}}\mathrm{d}\mu_{\mathrm{i}} \tag{27}$$

or simply using the molar transference number

$$\Phi(L) - \Phi(0) = -\frac{1}{F}\sum_i \int_0^L t_{\mathrm{i}}^*\mathrm{d}\mu_{\mathrm{i}} \tag{28}$$

The interface potentials can be derived from the condition of local equilibrium at the interface for which the electrochemical potential of each component must be equal in the neighboring phases. Thus, for equilibrium for the species i at an electrode A and an electrolyte S,

$$\mu_{\mathrm{i}}^{\mathrm{A}} + z_{\mathrm{i}}F\Phi^{\mathrm{A}} = \mu_{\mathrm{i}}^{\mathrm{S}} + z_{\mathrm{i}}F\Phi^{\mathrm{S}} \tag{29}$$

and the Galvanic potential difference at the interface is

$$\Phi^{\mathrm{S}} - \Phi^{\mathrm{A}} = -\left(\mu_{\mathrm{i}}^{\mathrm{S}} - \mu_{\mathrm{i}}^{\mathrm{A}}\right)/z_{\mathrm{i}}F \tag{30}$$

As an example, if cation $M^{+z_{\mathrm{M}}}$ and electrons carry the current in the electrolyte of the cell in Fig. 7, corresponding to the mixed conduction region close to the electronic domain, the voltage measured between electrode A and electrode B can be calculated by adding the two interface potentials (dependent on the reversibilities of electrodes A and B with respect to the $M^{+z_{\mathrm{M}}}$ ion) and the junction potential of Equation 27 in the electrolyte.

$$\begin{aligned} E = {} & [\Phi_{\mathrm{A}} - \Phi_{\mathrm{Cu^1}}] + [\Phi(0) - \Phi_{\mathrm{A}}] + [\Phi(L) - \Phi(0)] \\ & + [\Phi_{\mathrm{B}} - \Phi(L)] + [\Phi_{\mathrm{Cu^2}} - \Phi_{\mathrm{B}}] \end{aligned} \tag{31}$$

Substituting Equations 27 and 30 into Equation 31 and rearranging terms gives

$$\begin{aligned} E = \frac{1}{z_{\mathrm{M}}F}\Bigg[& \left(\mu^{\mathrm{A}}_{\mathrm{M}^{z_{\mathrm{M}}+}} + z_{\mathrm{M}}\mu_{\mathrm{e}}^{\mathrm{A}}\right) - \left(\mu^{\mathrm{B}}_{\mathrm{M}^{z_{\mathrm{M}}+}} + z_{\mathrm{M}}\mu_{\mathrm{e}}^{\mathrm{B}}\right) \\ & - \sum_i \frac{t_{\mathrm{i}}}{z_{\mathrm{i}}}\mathrm{d}\mu_{\mathrm{i}} + \left(\mu^{\mathrm{S(L)}}_{\mathrm{M}^{z_{\mathrm{M}}+}} - \mu^{\mathrm{S(0)}}_{\mathrm{M}^{z_{\mathrm{M}}+}}\right)\Bigg] \end{aligned} \tag{32}$$

where $\mu_{\mathrm{M}^{z_{\mathrm{M}}+}}$ is the chemical potential of $M^{z_{\mathrm{M}}+}$ ion and $\mu_{\mathrm{e}}^{\mathrm{Cu2}} = \mu_{\mathrm{e}}^{\mathrm{Cu1}}$ has been used. However, Equation 32 cannot be directly evaluated since the chemical potentials of electrically charged components are not measurable. Therefore, Equation 32 has to be rewritten in terms of the chemical potentials of electrically neutral components. Wagner [8] in 1933, derived the voltage of a Galvanic cell as a function of the chemical potential of neutral components. He used the concept of the chemical potential of the neutral metal species per equivalent, $\bar{\mu}_{[\mathrm{M}]}$, which is defined as $\mu_{[\mathrm{M}]}/z_{\mathrm{M}}$. This is related to the chemical potential of the metal ion, M, and the electron, e, by

$$\bar{\mu}_{[\mathrm{M}]} = \frac{1}{z_{\mathrm{M}}}\mu_{[\mathrm{M}]} = \frac{1}{z_{\mathrm{M}}}\mu_{\mathrm{M}^{z_{\mathrm{M}}+}} + \mu_{\mathrm{e}} \tag{33}$$

or simply

$$\bar{\mu}_{[M]} = \bar{\mu}_{M^{z_M+}} + \mu_e \tag{34}$$

where $\bar{\mu}_M \equiv (1/z_M)\mu_M$. Substituting Equation 34 in Equation 32 and rearranging terms, the voltage becomes

$$E = -\frac{1}{F}\left[\left(\bar{\mu}^B_{[M]} - \bar{\mu}^A_{[M]}\right) - \left(\bar{\mu}^S_{M^{z_M}} - \bar{\mu}^S_{M^{z_M}}\right) + \sum_i \int_0^L \frac{t_i}{z_i} d\mu_i\right] \tag{35}$$

Since $\sum_i t_i = t_M + t_e = 1$ holds, the second term in Equation 35 is evaluated as

$$\bar{\mu}^S_{M^{z_M+}}(L) - \bar{\mu}^S_{M^{z_M+}}(0) = \int_0^L (t_M + t_e) d\bar{\mu}_{M^{z_M+}} \tag{36}$$

Upon substituting Equation 36 into Equation 35 and using Equation 34, one obtains

$$E = -\frac{1}{F}\left[\left(\bar{\mu}^B_{[M]} - \bar{\mu}^A_{[M]}\right) - \int_0^L t_e d\bar{\mu}_{[M]}\right] \tag{37}$$

or simply

$$E = -\frac{1}{F}\int_0^L t_M d\mu_{[M]} \tag{38}$$

When the electrolyte has an electronic transference number equal to zero, i.e., it is a perfect ionic conductor over the range of μ_M spanned by the two electrodes, Equation 38 simply becomes the Nernst equation.

$$E = -\frac{1}{F}\left[\left(\bar{\mu}^B_{[M]} - \bar{\mu}^A_{[M]}\right)\right] = -\frac{RT}{z_M F}\ln\frac{a^B_M}{a^A_M} \tag{39}$$

where the activities of M in A and B must be referred to a common standard state.

5. Classification of electrochemical sensors

5.1. Potentiometric sensors

5.1.1. Type I sensor

The potentiometric sensor is one of the simplest chemical sensors based on the ion conducting properties of solid electrolytes. Consider the well known oxygen probe in cell (40) with an oxygen ion conductor, measuring in the high oxygen pressure regime where only oxygen ions and holes contribute to the conduction process.

$$(-)P'_{O_2}, O_2, Pt|O^{2-}, h^\bullet|Pt, O_2, P''_{O_2}(+) \tag{40}$$

In this case, the interface potential can be obtained from the local equilibrium reaction (41) occurring at the electrode/electrolyte/gas three-phase boundary involving the mobile O^{2-} ions in the electrolyte, electrons at the electrode and the O_2 gas component, in the ambient.

$$\frac{1}{2}O_2 + 2e = O^{2-} \tag{41}$$

At equilibrium, the sum of the electrochemical potentials on the right-hand side of Equation 41 must be equal to those of the left-hand side

$$\frac{1}{2}\mu_{O_2} + 2\tilde{\mu}_e = \tilde{\mu}_{O^{2-}} \tag{42}$$

Therefore, substituting Equation 23 into Equation 42 and rearranging terms provides the interface potential difference

$$\Phi^S - \Phi^{Pt} = \frac{1}{2F}\left(\mu^S_{O^{2-}} - \frac{1}{2}\mu_{O_2} - 2\mu^{Pt}_e\right) \tag{43}$$

where S and Pt stand for the electrolyte and Pt electrode, respectively. Then the cell voltage is given by the difference of the two interface potentials (each expressed as in Equation 43 at the Pt electrode/electrolyte phase boundaries) and the junction potential in the electrolyte, expressed as

$$E = (\Phi^{S'} - \Phi^{Pt}) - \frac{1}{F}\sum_i \int_{'}^{''} \frac{t_i}{z_i} d\mu_i + (\Phi^{Pt} - \Phi^{S''}) \tag{44}$$

where the superscripts $'$ and $''$ identify the left-hand and the right-hand boundaries of the electrolyte. Substituting Equation 43 in Equation 44, one obtains the voltage of the cell

$$E = \frac{1}{2F}\left[\left(\mu'_{O^{2-}} - \frac{1}{2}\mu_{O'_2} - 2\mu^{Pt}_e\right) - 2\sum_i \int_{'}^{'} \frac{t_i}{z_i} d\mu_i + \left(\frac{1}{2}\mu_{O''_2} + 2\mu^{Pt}_e - \mu''_{O^{2-}}\right)\right] \tag{45}$$

Because oxygen ions and holes are the only mobile species in the electrolyte, Equation 45 simplifies as

$$E = \frac{1}{2F}\left[\frac{1}{2}(\mu_{O''_2} - \mu_{O'_2}) - (\mu''_{O^{2-}} - \mu'_{O^{2-}}) + \int_{'}^{''} t_{O^{2-}} d\mu_{O^{2-}} - 2\int_{'}^{''} t_h d\mu_h\right] \tag{46}$$

Since $\mu''_{O^{2-}} - \mu'_{O^{2-}} = \int_{'}^{''}(t_{O^{2-}} + t_h)\, d\mu_{O^{2-}}$ and $\mu_{O^{2-}} + 2\mu_h = \frac{1}{2}\mu_{O_2}$, Equation 46 becomes

$$E = \frac{1}{4F}\left[(\mu_{O''_2} - \mu_{O'_2}) - \int_{'}^{''} t_h d\mu_{O_2}\right] \tag{47}$$

In view of the relation, $t_{O^{2-}} = 1 - t_h$, this is the same as

$$E = \frac{1}{4F}\int_{'}^{''} t_{O^{2-}} d\mu_{O_2} \tag{48}$$

When $t_h = 0$ (i.e., $t_{O^{2-}} = 1$), Equation 48 becomes the familiar Nernst equation for a concentration cell,

$$E = \frac{RT}{4F} \ln \frac{P_{O_2''}}{P_{O_2'}} \tag{49}$$

The chemical work, ΔG, in moving a mole of oxygen gas from the reference electrode to the sensing (working) electrode must be supplied by an electrical energy given as $-qE$, where q corresponds to the electron charge required by the electrochemical reaction. Hence $\Delta G = -qE$ holds, where $\Delta G = RT \ln P''_{O_2}/P'_{O_2}$ and $q = -4F$. Thus, the Nernst equation simply describes a reversible conversion from chemical to electrical energy.

Type I sensors are restricted to the detection of the species which correspond to the mobile ion species in the electrolyte. Though this restriction requires the use of an appropriate electrolyte, it makes the sensor inherently selective. Table II lists some known solid electrolytes for various ions.

5.1.2. Type II potentiometric sensor

Further flexibility in designing electrochemical sensors can be gained if an electrolyte exhibits a known equilibrium relationship between the chemical species to be detected and the component involving the mobile species in the electrolyte. In this case, the chemical potential of the conjugate (immobile) component in the electrolyte can be measured using an interpretation similar to a type I sensor.

For example, the Galvanic cell of type II arrangement in Fig. 8 can measure the SO_3 gas concentration, which is the immobile conjugate species in the silver-ion conducting Ag_2SO_4 electrolyte [32].

The acid-base equilibrium reaction (50) takes place in Ag_2SO_4 where Ag_2O and SO_3 are the basic and acidic components of the electrolyte, respectively.

TABLE II List of known ion-conducting electrolytes

Predominant conducting ion	Compounds	References
Fluorine (F^-)	CaF_2	[12, 13]
	MgF_2	[14]
	PbF_2	[15]
	NaF	[16]
	SrF_2	[14, 17]
Silver (Ag^+)	A- and β-AgI	[16, 18]
	AgCl	[16]
	AgBr	[16, 19, 20]
Oxygen (O^{2-})	$Zr_{1-x}M^{2+}_xO_{2-x}$	[21–23]
	$Zr_{1-x}M^{3+}_xO_{2-(x/2)}$	[21–23]
	$Th_{1-x}M^{2+}_xO_{2-x}$	[21, 22]
	$Th_{1-x}M^{3+}_xO_{2-(x/2)}$	[21–23]
Sodium (Na^+)	β-$Na_2O{\cdot}11Al_2O_3$	[24, 25]
	NASICON	[26]
Lithium (Li^+)	LIPON	[27]
	$Li_{1+x}\ Al_x\ Ti_{2-x}\ (PO_4)_3$	[28]
Proton (H^+)	$SrCe_{1-x}\ Yb_xO_3$	[29]
	$BaCe_{1-x}Gd_xO_3$	[30]
	$SrZr_{1-x}Y_xO_3$	[29]
	$CaZr_{1-x}In_xO_3$	[29]
	$BaZr_{1-x}Y_xO_3$	[31]

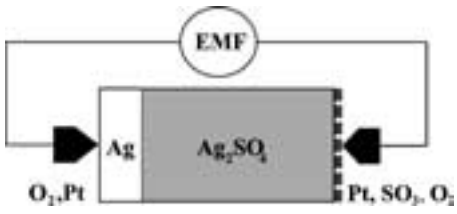

Figure 8 Schematic representation of an example type II arrangement. (−) Ag, O_2, $|Ag_2SO_4|$ Pt, SO_3, O_2 (+).

$$Ag_2O + SO_3 = Ag_2SO_4 \tag{50}$$

At the Pt working electrode, the equilibrium reaction (51) occurs

$$2Ag^+ + 2e^- + \frac{1}{2}O_2 = Ag_2O \tag{51}$$

to give

$$\Phi_{Pt} - \Phi_S = \frac{1}{2F}\left[2\mu_{Ag^+} + 2\mu_{e^-} + 1/2\mu_{O_2} - \mu_{Ag_2O}\right] \tag{52}$$

from the relation:

$$2\tilde{\mu}_{Ag^+} + 2\tilde{\mu}_{e^-} + 1/2\mu_{O_2} = \mu_{Ag_2O} \tag{53}$$

At the reference electrode of pure silver, the equilibrium reaction (54) occurs

$$Ag = Ag^+ + e^- \tag{54}$$

to give

$$\Phi_S - \Phi_{Ag} = \frac{1}{F}\left[\mu^\circ_{Ag} - \mu_{Ag^+} - \mu_e\right] \tag{55}$$

Since the chemical potential of the Ag^+ ion must be uniform in the electrolyte due to its high mobility and μ_{e^-} is the same for both electrodes, the emf can be obtained by adding Equations 52 and 55 to give

$$\Phi_{Pt} - \Phi_{Ag} = \frac{1}{2F}\left[2\mu^\circ_{Ag} + 1/2\mu_{O_2} - \mu_{Ag_2O}\right] \tag{56}$$

Upon substituting the relation $\mu_{Ag_2O} = \mu_{Ag_2SO_4} - \mu_{SO_3}$ into Equation 56, the emf of the cell is given as

$$E = -\frac{\Delta G^\circ_{Ag_2SO_4}}{2F} + \frac{RT}{2F} \ln\left[P_{SO_3} P_{O_2}^{1/2}\right] \tag{57}$$

where $\Delta G^\circ_{Ag_2SO_4}$ is the standard Gibbs free energy of formation and the activities of Ag and Ag_2SO_4 equal unity. Therefore, the cell emf has a logarithmic dependence on the concentration (partial pressure) of SO_3 in the ambient for a known oxygen partial pressure.

Likewise, the emf times the charge involved equals the work done on the system when a Ag^+ ion moves

spontaneously from the anode (Ag) to the cathode (Pt),

$$E = \frac{1}{F}\left(\mu^{\circ}_{Ag} - \mu_{Ag}\right) \tag{58}$$

where μ_{Ag} and μ°_{Ag} correspond to the chemical potential of silver in the silver sulfate in equilibrium with SO_3 and O_2 in the ambient and that of the pure silver reference electrode, respectively. The chemical potential of silver is determined by the reaction

$$Ag + \frac{1}{2}O_2 = Ag_2O \tag{59}$$

for a constant oxygen pressure in the air, and subsequently the chemical potential of Ag_2O becomes fixed by the acid-base equilibrium reaction (50). The same Equation 57 can be obtained by substituting Equations 50 and 59 into Equation 58.

5.1.3. Type III potentiometric sensor

The activity of the mobile component e.g., O_2 in YSZ, is measured with a type I arrangement. The type II electrochemical sensor enables one to measure the activities of immobile conjugate components in electrolytes such as Na_2CO_3, Na_2SO_4 and $AgNO_3$. However, type II sensors are still restricted by the limited number of suitable solid ionic conductors where a known equilibrium reaction exists with the species to be detected. When the electrolyte does not have a suitable immobile component, its activity cannot be detected in this way. To overcome this limitation, a type III sensor involves an electrode with an electronically conducting auxiliary phase and the same mobile ion as the electrolyte [9]. The electronic conductivity allows the chemical activity of the neutral component corresponding to the mobile ion to be uniform throughout the auxiliary phase. In the best case, the auxiliary phase should possess a high diffusivity or be porous. For the surface-modified type III electrochemical sensor in Fig. 9, the activities of Cl_2, NO_2, S_2 and CO_2 gases can be measured, using a Ag^+ conducting or a Na^+ conducting electrolyte with a corresponding gas-sensitive auxiliary layer of AgCl, $AgNO_3$ and $NaNO_3$, Ag_2S or Na_2CO_3, respectively [33].

The concentration of NO_2 can be measured with a cell (60) involving a type III electrode, adopting NASICON or β/β''-alumina as a Na^+-ion conducting electrolyte, $NaNO_3$ as an auxiliary phase and the mixture of Na_2ZrO_3 and ZrO_2 for a reference electrode [34].

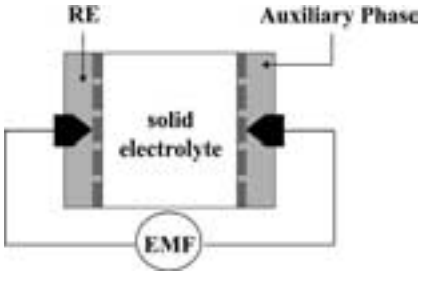

Figure 9 The schematic structure of type III arrangement.

$$(-)\mathrm{Au(Pt)},\ NaNO_3\ |Na^+|\ Na_2ZrO_3 + ZrO_2,\ \mathrm{Au(Pt)}(+) \tag{60}$$

The emf measured between the sensing (working) electrode and the reference electrode becomes

$$E = -\frac{1}{F}\left(\mu^{RE}_{Na} - \mu^{WE}_{Na}\right) = -\frac{RT}{F}\ln\frac{a^{RE}_{Na}}{a^{WE}_{Na}} \tag{61}$$

for $t_{Na^+} = 1$. The chemical activity of sodium at the sensing electrode in contact with the sodium nitrate auxiliary phase is fixed by the equilibrium

$$Na + NO_2 + \frac{1}{2}O_2 = NaNO_3 \tag{62}$$

for a given NO_2 and O_2 partial pressure, such that

$$a_{Na}(WE) = P^{-1}_{NO_2}P^{-1/2}_{O_2}\exp\left(\Delta G^{\circ}_{(62)}/RT\right) \tag{63}$$

where $\Delta G^{\circ}_{(62)}$ corresponds to the standard Gibbs free energy of reaction (62). In the reference electrode, the following equilibrium is maintained

$$2Na + \frac{1}{2}O_2 + ZrO_2 = Na_2ZrO_3 \tag{64}$$

to provide a fixed chemical activity of Na for a given oxygen pressure so that

$$a_{Na}(RE) = P^{-1/4}_{O_2}\exp\left(\Delta G^{\circ}_{(64)}/2RT\right) \tag{65}$$

where $\Delta G^{\circ}_{(64)}$ is the standard Gibbs free energy of reaction (64). Upon substituting Equations 63 and 65 into 61, one obtains the emf of the cell as

$$E = \frac{\Delta G^{\circ}_{(64)} - 2\Delta G^{\circ}_{(62)}}{2F} - \frac{RT}{F}\ln P_{NO_2} - \frac{RT}{4F}P_{O_2} \tag{66}$$

Therefore the emf of the cell (60) becomes logarithmically proportional to the NO_2 concentration (partial pressure) in the ambient for a given O_2 pressure (although the solid electrolyte itself does not involve NO_2).

5.1.4. Mixed potential potentiometric sensor

When more than one electrochemical reaction occurs at an electrode, the resulting electrode potential becomes a mixed potential which is generated from a competition of the various reactions occurring at the electrode. For example, when Au and Pt electrodes deposited on an yttria-stabilized zirconia electrolyte are exposed to an environment containing CO, CO_2 and oxygen as shown in Fig. 10, the oxygen reduction reaction,

$$O_2 + 4e^- \rightarrow 2O^{2-} \tag{67}$$

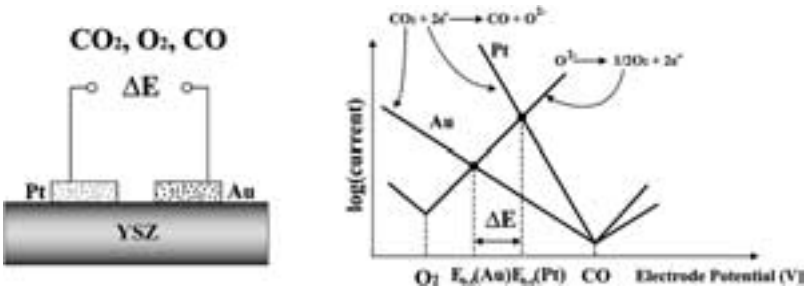

Figure 10 Schematic representation of a mixed potential sensor with polarization plots for the cathodic and anodic reactions [35].

occurs at a rate according to the Butler-Volmer equation

$$i_{O_2} = i^{\circ}_{O_2} \exp\left[-4\alpha_1 F\left(E - E^{\circ}_{O_2}\right)/RT\right] \quad (68)$$

and the corresponding carbon monoxide oxidation reaction,

$$CO + O^{2-} \rightarrow CO_2 + 2e^- \quad (69)$$

occurs simultaneously at a rate

$$i_{CO} = i^{\circ}_{CO} \exp[2\alpha_2 F\left(E - E^{\circ}_{CO}\right)/RT] \quad (70)$$

to give a mixed potential where the condition $i_{O_2} = i_{CO}$ is met. Therefore, assuming $i^{\circ}_{O_2} = k_1 P^{m}_{O_2}$ and $i^{\circ}_{CO} = k_2 P^{n}_{CO}$, the equilibrium mixed potential becomes

$$E_{mix} = E^{\circ} + [RT/(4\alpha_1 + 2\alpha_2)F]\left[m \ln P_{O_2} - n \ln P_{CO}\right] \quad (71)$$

where $E^{\circ} = \frac{RT}{F(4\alpha_1+2\alpha_2)} \ln \frac{k_2}{k_1} + \frac{2\alpha_1 E^{\circ}_{O_2} + \alpha_2 E^{\circ}_{CO}}{2\alpha_1+\alpha_2}$. For a constant oxygen partial pressure, the logarithmic dependence on P_{CO} is expressed as

$$E_{mix} = E'_0 + \beta \ln P_{CO} \quad (72)$$

where E'_0 and β are constants.

However, if E_{mix} is close to the equilibrium oxygen potential [36] so that the oxygen reduction reaction occurs at a low over-potential and the carbon monoxide oxidation reactions at high over-potential, the oxygen reduction kinetics may be represented by a Tafel-type equation, the low over-potential approximation of the Butler-Volmer equation:

$$i_{O_2} = i^{\circ}_{O_2} 4\alpha_1 F\left(E - E^{\circ}_{O_2}\right)/RT \quad (73)$$

The mass-transport-limited CO oxidation kinetics due to a high over-potential is described by:

$$i_{CO} = -2FAD_{CO}\frac{P_{CO}}{RT\delta} \quad (74)$$

where A and δ correspond to the electrode area and the width of the stagnant boundary layer, respectively. Combining Equation 73 with Equation 74 for $i_{O_2} = i_{CO}$ yields

$$E_{mix} = E^{\circ}_{O_2} - \frac{AD_{CO}}{2i^{O}_{O_2}\alpha_1\delta} P_{CO} \quad (75)$$

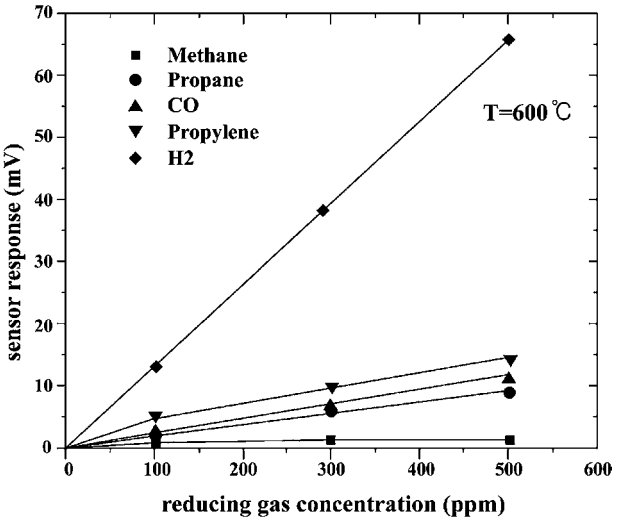

Figure 11 Voltage from differing electrode mixed potentials obtained from the cell Pt $|Ce_{0.8}Gd_{0.2}O_{1.9}|$ Au exposed to various reducing gases at 600°C [36].

which provides a linear relationship between CO concentration and the mixed potential, E_{mix}. Garzon *et al.* [36] observed a linear dependence of the mixed potential on the concentration of reducing gases for the cell Pt $|Ce_{0.8}Gd_{0.2}O_{1.9}|$Au in Fig. 11.

5.2. Amperometric sensor

The basic configuration of the amperometric electrochemical sensor, sometimes called limiting-current-type sensor, is shown in Fig. 12a. The working electrode of the zirconia cell has a pumping electrode inside an enclosure containing a small aperture or diffusion hole. When the electrode inside the enclosure is negatively biased, oxygen molecules are reduced at the cathode to form oxygen ions, which are then pumped to the anode outside the cell.

Depending on the ratio of pumping rate to the diffusion flux of oxygen through the aperture, three regions of I-V characteristics arise, as shown in Fig. 12b. According to Equation 26, the biasing voltage V obeys a relation

$$V = iR + (RT/4F) \ln P_{O_2}\left[(\text{ambient})/P_{O_2}(\text{cathode})\right] \quad (76)$$

At low voltage (region I) where the pumping rate is less than the diffusion flux, i.e., P_{O_2}(ambient) = P_{O_2}(cathode), the current increases linearly with the biasing voltage as $V = iR$. As the pumping rate

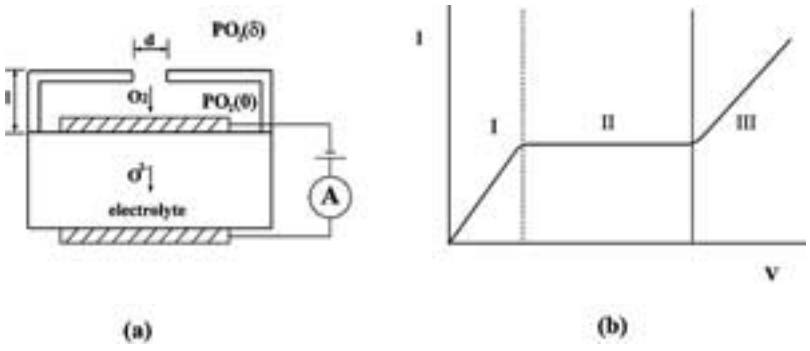

Figure 12 Schematic structure of an amperometric sensor and its typical response.

increases to exceed the diffusion flux of oxygen through the aperture, the current reaches a steady state (region II), which is determined by the rate of arrival of oxygen from the ambient through the hole to the electrode given as

$$J_{O_2} = i/4F = D_{O_2}\left[c_{O_2}(\delta) - c_{O_2}(0)\right]/\delta \approx \left[D_{O_2}P_{O_2}\right]/[RT\delta] \quad (77)$$

where δ corresponds to the effective diffusion distance for oxygen and $c_{O_2} = P_{O_2}/RT$ has been used. If the biasing voltage is large enough (normally 0.5–1.5 V), the oxygen partial pressure at the cathode will decrease to nearly zero, $c_{O_2} \approx 0$, which gives the last term in Equation 77. Hence, the pumping current at steady state depends linearly on the oxygen partial pressure in the ambient. Sometimes this sensor is called "a proportional oxygen gauge," adopted to monitor lean-burn automobile engines. However, from Equation 76, the increase in voltage is compensated by a decrease in oxygen pressure at the cathode for a constant value of the limiting current. As the biasing voltage increases to the region III where the oxygen partial pressure becomes lower than about 10^{-33} atm [37], electronic conduction rises to give a further increase in current by the decomposition reaction, $O_O^{\times} \rightarrow V_O^{\bullet\bullet} + 1/2O_2 + 2e'$. In practice, the limiting current type sensor is operated in region II where the steady state current can be obtained.

Depending on the size of the aperture, the diffusion of gas can be characterized as ① a bulk diffusion process or ② a Knudsen diffusion process [38]. Bulk diffusion occurs when the aperture diameter d is much greater than the mean free path λ of the gas molecules, such that the frequency of molecule-wall collisions is negligible compared with intermolecular collisions in the free space. At atmospheric pressure, this corresponds to the hole diameter greater than about 10^5 Å. According to the simple gas kinetic model for rigid spherical molecules [39], the bulk diffusion coefficient (cm/s^2) of gas 1 in gas 2 is given as

$$D_1^2 = 2.6 \times 10^{-3}[T^3(M_1 + M_2)/2M_1M_2]^{1/2}/(P_T\sigma_{12}) \quad (78)$$

which is inversely proportional to the total pressure and directly proportional to $T^{3/2}$. In the presence of intermolecular interaction, the value of the power factor in T is between 1.5 and 2. Experimentally, $T^{1.7}$ has been obtained [40].

In a very small channel (less than ≈100 Å) where $d/\lambda \ll 1$, gas diffuses by Knudsen diffusion whose coefficient D_K is one to two orders of magnitude smaller than the bulk diffusivity D_1^2. The Knudsen diffusion coefficient has been derived for a cylindrical channel of radius a from the kinetic theory of gases as [41]

$$D_K = \frac{2}{3}a[8RT/\pi M]^{1/2} \quad (79)$$

which is independent of total pressure within the free molecular flow regime and proportional to the square root of T.

For an intermediate pore radius (10^2–10^5 Å), in which both intermolecular collisions in the gas and wall collisions impede the gaseous diffusion, a mixed diffusion behavior is expected, with the resulting diffusivity of $1/D = 1/D_1^2 + 1/D_K$.

The bulk diffusion flux of oxygen through the aperture at steady state can be written, in terms of Fick's 1st law, as [42]

$$J_{O_2} = -D_{O_2}\frac{dc_{O_2}}{dx} + X_{O_2}J_{O_2} \quad (80)$$

where D_{O_2}, c_{O_2} and X_{O_2} are the bulk diffusivity, the molar concentration ($mole/cm^3$) and the mole fraction of oxygen molecules, respectively. The second term in Equation 80 corresponds to the convection flux resulting from the pressure gradient along the diffusion path. For the total convection flux J_{O_2} in the cavity, including other gases to balance out the pumping current, it is assumed that X_{O_2} is the oxygen mole fraction. This can be solved for the boundary conditions

$$x = 0 \quad c_{O_2} = X_{O_2}\ \text{(ambient)}$$
$$x = l \quad c_{O_2} = X_{O_2}(0) \ll X_{O_2}\ \text{(ambient)}$$

to give the limiting current density arising from bulk diffusion through the aperture

$$i_{lim} = 4FJ_{O_2} = -\frac{4FD_{O_2}P_T}{RTl}\ln\left(1 - X_{O_2}\right) \quad (81)$$

where l, F, and P_T are the length of the diffusion hole, the Faraday constant, and the total pressure in the

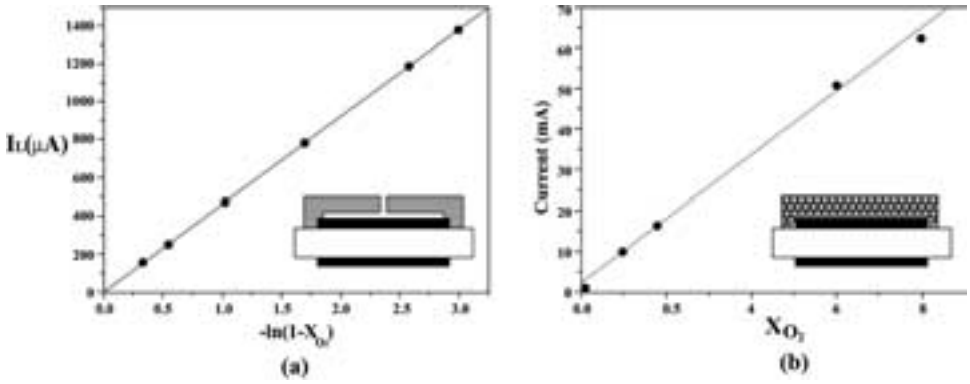

Figure 13 (a) Limiting currents for bulk diffusion ($P_T = 1$ atm, $T = 500°C$, O_2–N_2 gas) [43]. (b) Limiting currents for the Knudsen diffusion process in a sol-gel diffusion barrier [44].

ambient; again, the relation $c_{O_2} = X_{O_2} P_T / RT$ has been used. When the rate-limiting step is the bulk diffusion of oxygen through the aperture, the limiting current density becomes proportional to $-\ln(1 - X_{O_2})$, independent of the total pressure and proportional to $T^{-0.5}$ because of the relation, $D \propto T^{1.5}/P_T$.

Similarly, the Knudsen diffusion flux can be written as

$$J_{O_2} = -D_{O_2} \frac{dc_{O_2}}{dx} \tag{82}$$

where the convection flux due to the pressure gradient in Equation 80 has been omitted because, in the Knudsen regime, the wall resistance to the convection flow is so large that the convection flux becomes negligible. From Equation 82 for the same boundary conditions, the limiting current density becomes

$$i_{lim} = 4FJ_{O_2} = -\frac{4FD_{O_2} P_T}{RTl} X_{O_2} \tag{83}$$

As $D_{O_2} \propto T^{1/2}$ from Equation 79, the limiting current density in the Knudsen regime becomes proportional to the total pressure and $T^{-0.5}$. The dependences of the limiting currents on $-\ln(1 - X_{O_2})$ and X_{O_2} for bulk diffusion and for Knudsen diffusion, respectively, are shown in Fig. 13.

6. Designing an electrochemical sensor

6.1. Electrolyte selection

In potentiometric electrochemical sensors, the maximum range of detection is often decided by the width of the electrolytic domain for the electrolyte. When the electrolyte exhibits electronic as well as ionic conductivity, the emf obtained deviates from the theoretical value. Schmalzried [45, 46] first treated theoretically the measured emf of a galvanic cell involving reversible electrodes and mixed conducting electrolyte. For a mixed conducting oxide electrolyte, he assumed P_{O_2}-independent $\sigma_{O^{2-}}$ and constant carrier mobilities for the hole and electron. These quantities obey relations of $\sigma_p = \sigma_{O^{2-}}(P_{O_2}/P_\oplus)^{1/n}$ and $\sigma_n = \sigma_{O^{2-}}(P_{O_2}/P_\ominus)^{-1/n}$, respectively. Hence $t_{O^{2-}}$ in the mixed conducting oxygen electrolyte can be written as

$$t_{O^{2-}} = \sigma_{O^{2-}}/[\sigma_{O^{2-}} + \sigma_p + \sigma_n] = \left[1 + \left(\frac{P_{O_2}}{P_\oplus}\right)^{1/n} + \left(\frac{P_{O_2}}{P_\ominus}\right)^{-1/n}\right]^{-1} \tag{84}$$

where $P_\oplus$ and $P_\ominus$ are oxygen pressures for $\sigma_{O^{2-}} = \sigma_p(t_{O^{2-}} = 0.5)$ and $\sigma_{O^{2-}} = \sigma_n(t_{O^{2-}} = 0.5)$, respectively, and n is a constant. Substituting Equation 84 into Equation 48 and integrating, Schmalzried obtained the general relation for the cell emf:

$$E = -\frac{nRT}{4F}\left[\ln \frac{P_\oplus^{1/n} + P_{O_2}(WE)^{1/n}}{P_\oplus^{1/n} + P_{O_2}(RE)^{1/n}} + \ln \frac{P_\ominus^{1/n} + P_{O_2}(RE)^{1/n}}{P_\ominus^{1/n} + P_{O_2}(WE)^{1/n}}\right] \tag{85}$$

for the condition of a wide electrolytic domain with $P_\ominus/P_\oplus \ll 1/4$, where $P_{O_2}(RE)$ corresponds to P_{O_2} at the reference electrode and $P_{O_2}(WE)$ at the sensing electrode.

Consider a case where the oxygen partial pressure at the reference electrode is fixed so low that an electronic conduction becomes dominant, i.e., $P_{O_2}(RE) \ll P_\ominus$. The Nernst relation says that the theoretical (or ideal) emf values have to be written as $E = \frac{RT}{4F} \ln(P_{O_2}(WE)/P_{O_2}(RE))$. However, according to Equation 85, three different forms of emf values arise depending on the oxygen partial pressure at the sensing electrode:

① when $P_{O_2}(WE)$ is in the electronic conduction domain, i.e., $P_{O_2}(WE) \ll P_\ominus$, the emf becomes, $E = 0$ from Equation 85

② when $P_{O_2}(WE)$ is in the ionic conduction domain, i.e., $P_\oplus \gg P_{O_2}(WE) \gg P_\ominus$, the emf becomes, $E = -\frac{RT}{4F} \ln(P_\ominus/P_{O_2}(WE))$

③ when $P_{O_2}(WE)$ is in the domain of hole conduction, i.e., $P_{O_2}(WE) \gg P_\oplus$, the emf becomes, $E_\infty = -\frac{RT}{4F} \ln P_\ominus/P_\oplus$, which is constant for a given electrolyte.

A graphical representation for the case of $P_{O_2}(RE) \ll P_\ominus$ is shown in Fig. 14 where Curve ① and ②

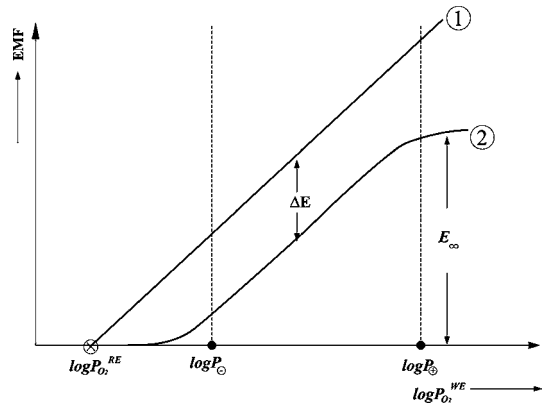

Figure 14 Cell emf as a function of log $P_{O_2}(WE)$ for a fixed value of log $P_{O_2}(RE)$ where $P_{O_2}(RE)$ is in the electronic conduction domain, i.e., $P_{O_2}(RE) \ll P_\ominus$ ①: $E = RT/4F \ln[P_{O_2}(WE)/P_{O_2}(RE)]$, ②: measured emf $\Delta E = RT/4F \ln[P_\ominus/P_{O_2}(RE)]$, $E_\infty = RT/4F \ln[P_\oplus/P_\ominus]$ [45].

correspond to the Nernstian and the measured emf, respectively. When $P_{O_2}(WE) < P_\ominus$, the measured emf is close to zero volt. The cell emf becomes a constant value of $E_\infty = \frac{RT}{4F} \ln P_\oplus/P_\ominus$ for $P_{O_2}(WE) > P_\oplus$. From Fig. 14 an error signal of $\Delta E = \frac{RT}{4F} \ln(P_\ominus/P_{O_2}(RE))$ occurs for the measurement of oxygen pressure at the measuring electrode in the regime of the electrolytic domain even though it gives Nernstian slope. The measured emf becomes coincident with the Nernstian value only when both electrodes reside within the electrolytic conduction-domain boundaries, i.e., $P_\ominus \ll P_{O_2}(WE)$, $P_{O_2}(RE) \ll P_\oplus$. The theory assumes that the electrodes remain reversible despite the inherent internal passage of oxide ions resulting from mixed conduction.

6.2. Cross-sensitivity

Selective detection is an important advantage of an electrochemical sensor, but sometimes their responses are affected by the presence of other gases. Cross-sensitivity is often observed when type II or type III potentiometric sensors are exposed to gas species that form thermodynamically more stable compounds, or kinetically more favorable compounds in spite of lower thermodynamic stability [47].

For instance, the application of AgCl as a surface modifying layer in type III sensor is very advantageous from the point of view of the high stability of AgCl. However, Ag_2SO_4 is thermodynamically more stable such that even a trace of SO_2 should result in the formation of Ag_2SO_4. As shown in Fig. 15, at partial pressures of Cl_2 and SO_2 above the equilibrium lines for various temperatures, Ag_2SO_4 should be formed, whereas AgCl is stable below these lines. Fortunately, the formation of Ag_2SO_4 is kinetically unfavorable such that AgCl will persist in spite of its lower stability, unless SO_2 is sufficiently abundant in the ambient.

On the contrary, the formation of Ag_2S is kinetically favorable because a large number of silver defects with high mobility which allow the fast formation of this compound. A major cross-sensitivity for the chlorine sensor occurs as shown in Fig. 16, because Ag_2S forms upon exposure of a AgCl surface modifying layer to

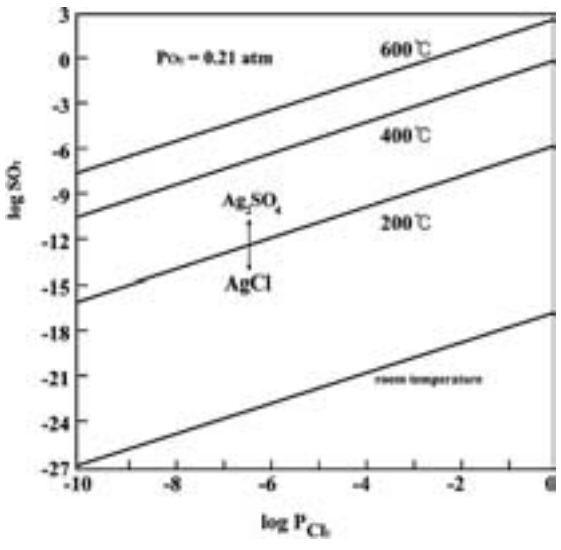

Figure 15 Thermodynamic stabilities of Ag_2SO_4 and AgCl at various temperatures [47].

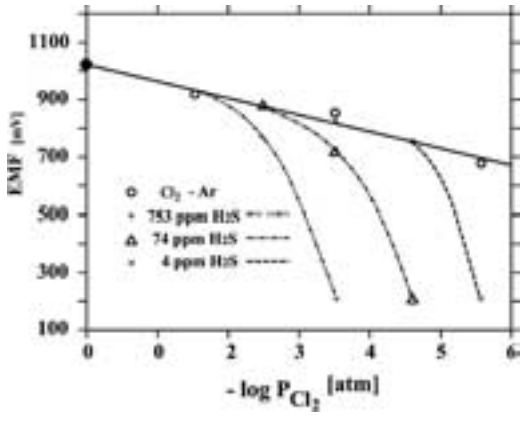

Figure 16 Cross-sensitivity of a Cl_2 sensor to H_2S [48].

H_2S gas, in spite of the lower Ag_2S stability compared to AgCl. A decrease in the cell voltage is observed when the H_2S partial pressure approaches the Cl_2 partial pressure, in fact, at a H_2S concentration of about 10% of the Cl_2 pressure [48]. In this case, the cell voltage is established by the formation of Ag_2S, and any further reaction toward the more stable AgCl does not occur anymore. The influence of H_2S is critical to the interpretations because the voltage drop simulates a lower chlorine concentration than really exists.

6.3. Reference electrode

The reference electrode material should be chemically stable and reversible at the operating temperature and in the measurement atmosphere. For example, the mixed reference material of $Na_2Ti_6O_{13}$ and TiO_2 usually used for the carbon dioxide sensor to fix the activity of Na_2O does not form sodium carbonate when it is exposed to an environment containing carbon dioxide gas because the Gibbs free energy of the reaction

$$Na_2CO_3 + 6TiO_2 = Na_2Ti_6O_{13} + CO_2 \qquad (86)$$

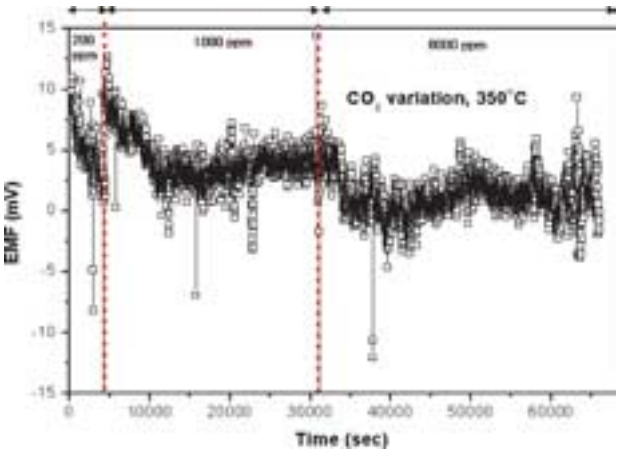

Figure 17 The variation of EMF with changing CO_2 concentration for the cell $Na_2Ti_6O_{13}$, TiO_2, Pt |NBA| Pt, Na_2ZrO_3, ZrO_2.

is negative in the detection range of CO_2 whereas the reaction, $Na_2CO_3 + ZrO_2 = Na_2ZrO_3 + CO_2$ has positive energy change. Formation of sodium carbonate on Na_2ZrO_3/ZrO_2 mixture makes the sensor eventually respond to the change of CO_2 concentration as shown in Fig. 17.

7. Applications

7.1. Oxygen sensor

7.1.1. Potentiometric sensor

One of the most successful applications of an electrochemical sensor is found in the exhaust emission control system for the automobile engine. Since the strict regulation of air pollution in California in 1965, all gasoline-burning cars are equipped with a catalytic converter comprising of finely dispersed noble metal catalyst (Pt, Pd, Rh) dispersed on a ceramic support. The three regulated exhaust toxic pollutants NO_x, HC, and CO are eliminated by more than 90% by the catalytic converter and, hence, is referred to as a three-way catalyst (TWC). The best performance of the TWC is obtained for an equivalent air/fuel ratio ($\lambda = A/F$) equal to one (weight ratio of air to fuel = 14.6), which can be monitored by the detection of the oxygen content in the exhaust gas upstream from the catalytic converter.

The oxygen sensor, sometimes called EGO (Exhaust Gas Oxygen) or lambda sensor, is a potentiometric (type I) sensor generally comprising an yttria-stabilized zirconia electrolyte with air reference ($P_{O_2} = 0.21$ atm) as shown in Fig. 18a. The oxygen partial pressure in the exhaust gas changes by several orders of magnitude in the vicinity of stoichiometric combustion, which, in turn, gives an abrupt decrease in emf (more than 0.5 V) when it crosses from fuel rich to fuel lean, as shown in Fig. 18b. In practice, engines are operated at 0.45 V.

7.1.2. Anomalous behavior

In principle, the oxygen sensor measures the oxygen partial pressure for the equilibrium electrochemical reaction occurring at the sensing electrode,

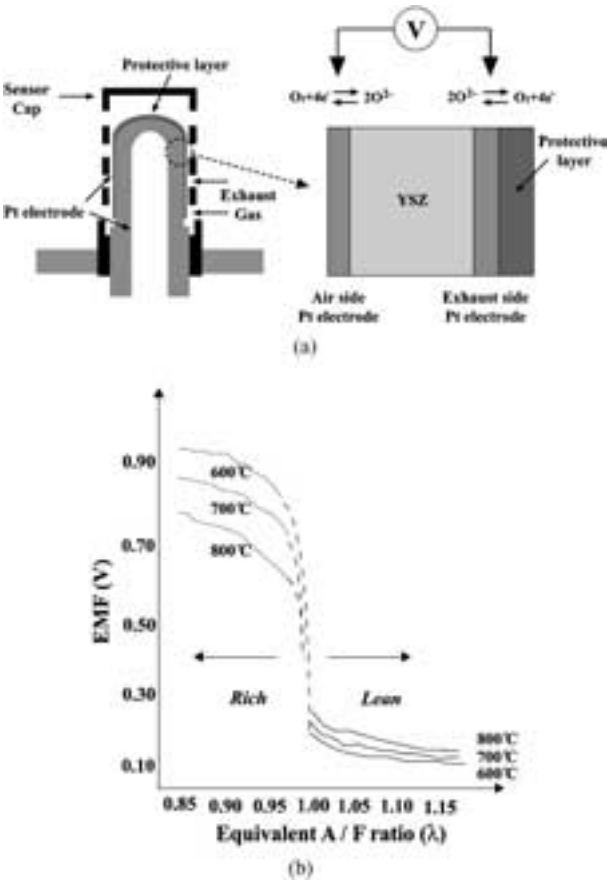

Figure 18 Cross-sectional view of an EGO sensor with its output characteristics [49]. (a) the sensor geometry and (b) emf response.

$$\frac{1}{2}O_2 + 2e = O^{2-} \tag{87}$$

where the lattice oxygen ions in the zirconia electrolyte are in equiibrium with adsorbed oxygen species at the three phase boundaries of zirconia, electrode and gas. However, when the concentration of oxygen in an exhaust gas containing various reducing species is measured, the response is often affected by various competing chemical reactions [50]:

$$2NO = N_2 + O_2 \tag{88}$$

$$NO + 1/2O_2 = NO_2 \tag{89}$$

$$CO + 1/2O_2 = CO_2 \tag{90}$$

$$(HC)_n + (5n/4)O_2 = (n/2)H_2O + nCO_2 \tag{91}$$

or by electrochemical reactions occurring at the electrode:

$$2NO + 4e^- = N_2 + 2O^{2-} \tag{92}$$

$$NO + O^{2-} = NO_2 + 2e^- \tag{93}$$

$$CO + O^{2-} = CO_2 + 2e^- \tag{94}$$

$$(HC)_n + (5n/2)O^{2-} = (n/2)H_2O + nCO_2 + 5ne^- \tag{95}$$

The kinetics of these reactions depend on temperature and the electrode materials. For example, at high temperature (>600°C), reaction (87) is generally far faster than the electrochemical reactions (92)–(95). However, the kinetics of the chemical reactions (88)–(91) are relatively fast on the highly catalytic electrodes of Pd, Rh and Pt. But these reactions are rather slow on a low-catalytic electrode such as Au and Ag. Hence, when Pt is used as a sensing electrode for the zirconia oxygen sensor, it does not measure the oxygen content existing in the non-equilibrium exhaust gas, but rather the oxygen concentration that the exhaust gas would have if it were in internal thermodynamic equilibrium. For this reason, the EGO is sometimes called "an equilibrium electrode."

On the other hand, when low-catalytic sensing electrodes are used, they measure the actual oxygen content in the non-equilibrium exhaust gas, i.e., $P_{O_2}^{\text{electrode}} = P_{O_2}^{\text{gas}}$ due to the negligible extent of chemical reaction at the electrode surface. Therefore this is called "an oxygen electrode" instead.

At moderate temperature (500–600°C), where the rates of electrochemical reactions (92)–(95) are comparable to that of reaction (87), the steady cell voltage responds to the mixed potential established by the competition between reactions (92)–(95) and reaction (87). In this case, the oxygen partial pressure and the electrochemical potential of the O^{2-} ion in reaction (87) are decided jointly by the chemical equilibria of reactions (88)–(91) and the electrochemical reactions (92)–(95), respectively. These emfs generally deviate from the theoretical value of the Nernst law.

Many zirconia oxygen sensors do not exhibit ideal performance in the presence of other gases such as H_2, CO, NO and hydrocarbons. For instance, the shift in the voltage step shown in Fig. 19a toward the lean region was observed for non-equilibrium combustion gases containing hydrogen [51] and CO [52]. In this case, the H_2 and CO reactant species in the exhaust gas mixture diffuse through the porous protective layer faster than oxygen without reaching chemical equilibrium before the catalytic reaction occurs at the Pt electrode, as shown in Fig. 19b. Therefore the oxygen concentration near the electrode becomes much lower than the equilibrium P_{O_2} (for the bulk ambient), which results in a sensor output shifted to the lean region.

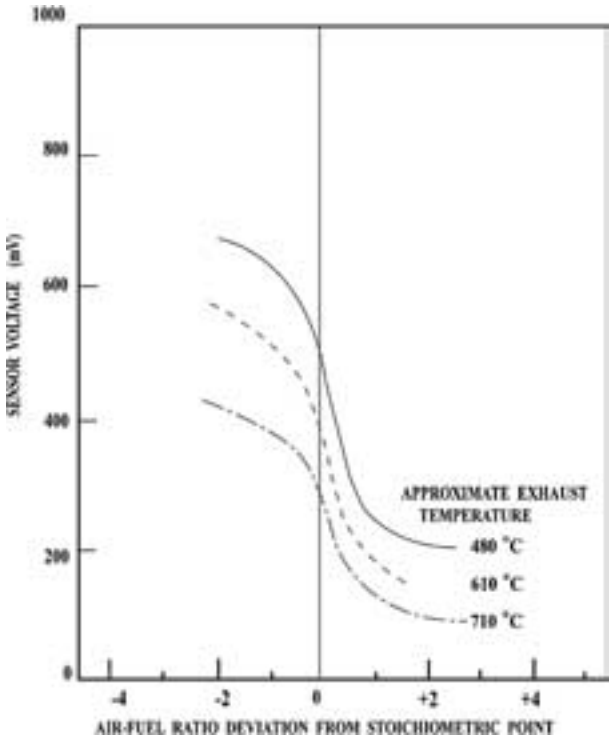

Figure 20 Non-ideal "washed-out" performance of oxygen sensor [53].

Sometimes, an oxygen sensor signal provides a "washed-out" curve, especially, in the presence of CO as shown in Fig. 20. Fleming [53] considered the competitive adsorption of CO and O_2 at the active triple points of the Pt anode with site fractions of f_{CO} and f_{O_2}, respectively. It was assumed that CO adsorption follows the Langmuir isotherm, and the remaining sites are occupied by oxygen such that $f_{CO} = K_{CO}p_{CO}/(1 + K_{CO}p_{CO} + K_{O_2}p_{O_2})$ and $f_{O_2} = 1 - f_{CO}$. The simultaneous presence of adsorbed CO and O_2 creates an effect of two independent galvanic cells in the

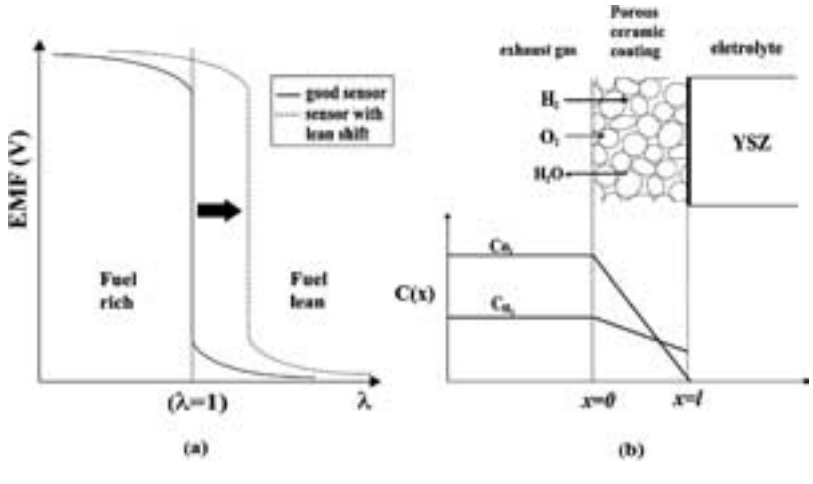

Figure 19 The shift in stoichiometric combustion to a leaner composition in the presence of hydrogen [51]: (a) lean shift (b) concentration profiles of oxygen and hydrogen in the protective layer.

total sensor output voltage, with the respective emf given as

$$E_{O_2} = E^{\circ}_{O_2} + \frac{RT}{4F} \ln \left(\frac{P_{O_2}(\text{air})}{P_{O_2}(\text{anode})} \right) \quad (96)$$

for the oxygen cell where $E^{\circ}_{O_2}$ arises from the inhomogeneity of electrodes, and

$$E_{CO} = E^{\circ}_{CO} + \frac{RT}{4F} \ln \left(\frac{P^{1/2}_{O_2}(\text{air}) P_{CO}(\text{anode})}{P_{CO_2}(\text{anode})} \right) \quad (97)$$

from Equation 90 for CO the cell, where $E^{\circ}_{CO} = \frac{1}{2F}[\mu^{\circ}_{CO}(\text{anode}) - \mu^{\circ}_{CO_2}(\text{anode}) + \frac{1}{2}\mu^{\circ}_{O_2}(\text{cathode})]$. The resulting voltage can be expressed as

$$E = f_{O_2} E_{O_2} + f_{CO} E_{CO} \quad (98)$$

Substituting equilibrium p_{O_2}. p_{CO} and p_{CO_2} corresponding to the A/F ratio in Equations 96, 97 and 98, a rich and lean voltage tail to the output curve similar to Fig. 20 was obtained.

7.1.3. Ameprometric/limiting current sensor

The stoichiometric point in the combustion process can be successfully measured with a potentiometric type oxygen sensor, as shown in Fig. 18. However, when one must measure a high concentration of oxygen such as in the lean combustion gas (far from the stoichiometric composition), the potentiometric measurement is difficult because, according to Equation 96, the voltage depends linearly on the temperature but only logarithmically on the oxygen pressure, which ordinarily requires a precise temperature control for sensing. Therefore, a limiting current measurement that gives a linear dependence on oxygen concentration is preferable for the detection of wide range of high oxygen concentrations.

One of limiting-current oxygen sensors is a wide range air/fuel ratio sensor (sometimes called the UEGO sensor). There are many variations of structural design [54–56], but it generally consists of a sensing cell and a pumping cell as shown in Fig. 21. The emf of the sensing cell is normally fixed at 300–450 mV with respect to the air reference, which gives an oxygen pressure of about 10^{-7}–10^{-10} atm in the cavity at 800°C. The current that must pass through the pumping cell to maintain a constant oxygen pressure (10^{-7}–10^{-10} atm) in the sensing cell is used as an output of the sensor [57–60]. In the oxidizing atmosphere of a lean combustion gas, oxygen has to be pumped out to reduce the oxygen pressure in the cavity as shown in Fig. 21a. On the contrary, in the fuel-rich region, where abundant reducing species such as CO and hydrocarbon exist, the pumping direction has to be reversed to raise the oxygen pressure in the cavity as in Fig. 21b. In this case, CO in the exhaust gas plays an important role in the limiting current [57–60]. The pumped oxygen is consumed in the cavity according to Equation 95 such that the rate of arrival of CO determines the limiting current. The constant value of limiting current in Equation 76 is obtained by decreasing the biasing voltage to compensate for the increase in oxygen pressure within the cavity. The value of the response current shows a gradual increase as the fuel changes from rich to lean, as shown in Fig. 21c, contrasting to the step response of the lamda sensor. The slope in the fuel-rich region is higher than that in the lean region because the reducing species such as hydrogen and CO present in the fuel-rich gas must be oxidized at the pumping electrode to maintain a given oxygen pressure in the cavity.

7.2. Carbon dioxide sensor

Carbon dioxide sensing has become important in many applications. Carbon dioxide gas emitted from automobiles and factories burning coal and hydrocarbons is recognized as a major cause of the global warming of the earth. Hence monitoring CO_2 in the atmosphere is important to track the status of the environment. Monitoring CO_2 plays an important role in the storage of fresh agricultural products such as fruits and meats (e.g., Modified Atmosphere Packaging (MAP)). MAP system prevents the drip loss problem and improves the color stability of meat. Moreover, decreased oxygen and increased CO_2 concentrations reduce the respiration rate of fruit. Furthermore, CO_2 plays important role in controlling corrosion rate in chemical processing and carbonation of concrete.

Optical absorption of infrared has been used to measure the concentration of CO_2. It can successfully measure CO_2 from a few % to more than 70%, but the sensitivity of the photodiode makes it practically impossible to detect CO_2 concentrations lower than a few hundred ppm. Moreover, the optical system is generally vulnerable to a hostile environment, which limits its use to indoor and remote sensing applications. In

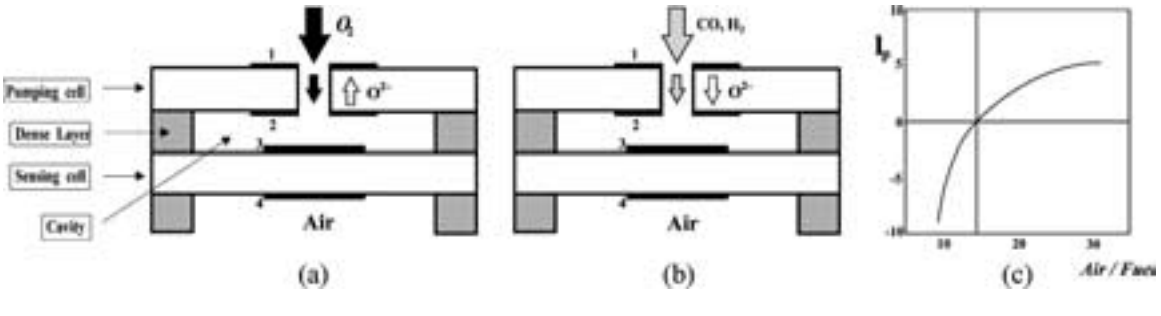

Figure 21 The schematic illustration of the wide range oxygen sensor (a, b) and its pumping current response with A/F ratio (c). (a): Lean exhaust gas (b): Rich exhaust gas (c): Pumping current response with A/F ratio.

contrast, electrochemical detection of CO_2 enjoys the advantages of low cost and in-situ monitoring capability. Potentiometric sensors adopting type II [61–63] and type III [64–68] cells have been widely studied.

The first potentiometric CO_2 sensor was proposed by Gauthier [58] using a type II cell with a K_2CO_3 electrolyte.

$$\text{Pt, } O_2', CO_2' \,|K_2CO_3|\, CO_2'', O_2'', \text{Pt} \qquad (99)$$

Later, Maruyama *et al*. [66] adopted a type III cell (109) with sodium conducting electrolytes such as NASICON and Na-β-alumina (NBA).

$$(-)\text{Au, } O_2, \;|\text{NASICON}|\; Na_2CO_3, CO_2, O_2, \text{Au}(+) \qquad (100)$$

In this galvanic cell, the anode and cathode reactions are:

$$Na_2CO_3 = 2Na^+ + CO_2 + 1/2O_2 + 2e^- \qquad (101)$$

and

$$2Na^+ + CO_2 + 1/2O_2 + 2e^- = Na_2O(\text{NASICON}) \qquad (102)$$

Hence, the total cell reaction becomes

$$Na_2CO_3 = Na_2O + CO_2(g) \qquad (103)$$

and the emf of the cell (100) can be written as

$$E = E^\circ - \frac{RT}{2F} \ln\left[P_{CO_2} a_{Na_2O}^{\text{NASICON}}\right] \qquad (104)$$

where $E^\circ = -\Delta G^\circ_{(103)}/2F$. Apparently, Equation 104 has a logarithmic dependence on both the CO_2 concentration in the ambient as well as of the chemical activity of Na_2O in the NASICON, which depends on the amount of Na added in the compound.

This cell has been further improved through modification of the cathode to provide a fixed a_{Na_2O} using solid reference mixtures such as Na_2SnO_3/SnO_2, $Na_2Ti_6O_{13}/TiO_2$ and Na_2ZrO_3/ZrO_2 [65], e.g.

$$\text{Au, } O_2, Na_2Ti_6O_{13}, TiO_2|Na^+\text{conductor}|Na_2CO_3, \; CO_2, O_2, \text{Au} \qquad (105)$$

These sensors can be fabricated either in bulk structure or planar structure using thick film technology, as shown in Fig. 22.

In the Galvanic cell (105), the Na_2O activity in the reference electrode is fixed by the equilibrium relation between the pure phase of TiO_2 and $Na_2Ti_6O_{13}$

$$6TiO_2 + Na_2O = Na_2Ti_6O_{13} \qquad (106)$$

which gives the Na_2O activity as

$$a_{Na_2O} = \exp\left(\Delta G^\circ_{(106)}/RT\right) \qquad (107)$$

Substituting Equation 107 into Equation 104, the voltage measured from the cell (105) becomes a function of only the partial pressure of carbon dioxide expressed as

$$E = E^\circ - \frac{RT}{2F} \ln P_{CO_2} \qquad (108)$$

where $E^\circ = -(\Delta G^\circ(103) + \Delta G^\circ(106))/2F$. Note that a_{Na_2O} in Equation 104 is not involved. Furthermore, $\Delta G^\circ(103) + \Delta G^\circ(106)$ corresponds to $\Delta G^\circ_{(109)}$, the change in the standard Gibbs free energy for the reaction:

$$Na_2CO_3 + 6TiO_2 = Na_2Ti_6O_{13} + CO_2 \qquad (109)$$

Fig. 23 shows the typical emf response of the cell (105) upon changing CO_2 concentration from 200 ppm to 20,000 ppm and back to 200 ppm, and its concentration dependence that obeys the theoretical slope of $-RT/2F$ as in Equation 108.

7.2.1. Selection of electrolyte

The Na^+ ion conducting electrolytes such as Na_2CO_3 [63], NASICON [66, 68, 69] and Na-β-alumina [64, 65] and Li^+ ion conducting electrolytes such as lithium phosphorous oxynitride ($Li_{2.88}PO_{3.73}N_{0.14}$) [27, 70] and $LiTi_2(PO_4)_3 + 0.2Li_3PO_4$ [71] are widely used in CO_2 sensors. NASICON is a silico-phosphate of composition $Na_{1+x}Zr_2Si_xP_{3-x}O_{12}(0 < x < 3)$, which shows a maximum conductivity at $x \approx 2$. The β-alumina has a structure of $(Na_2O)_{1+x} \bullet 11Al_2O_3$, where the maximum conductivity occurs at $x = 0.2$–0.3 [72].

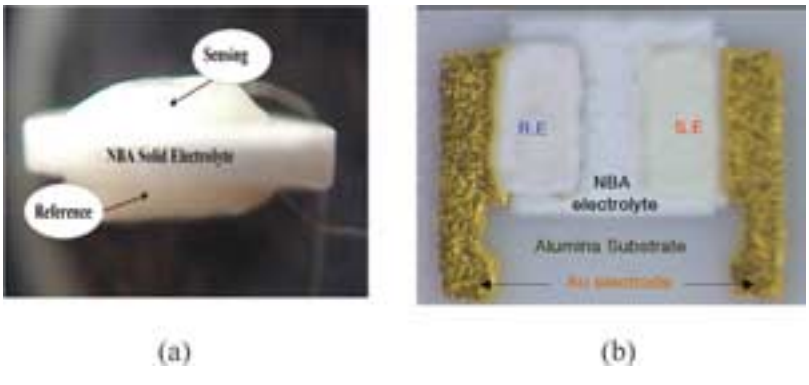

Figure 22 Potentiometric CO_2 sensors of (a) bulk type and (b) thick film type (2.5 mm × 2.5 mm).

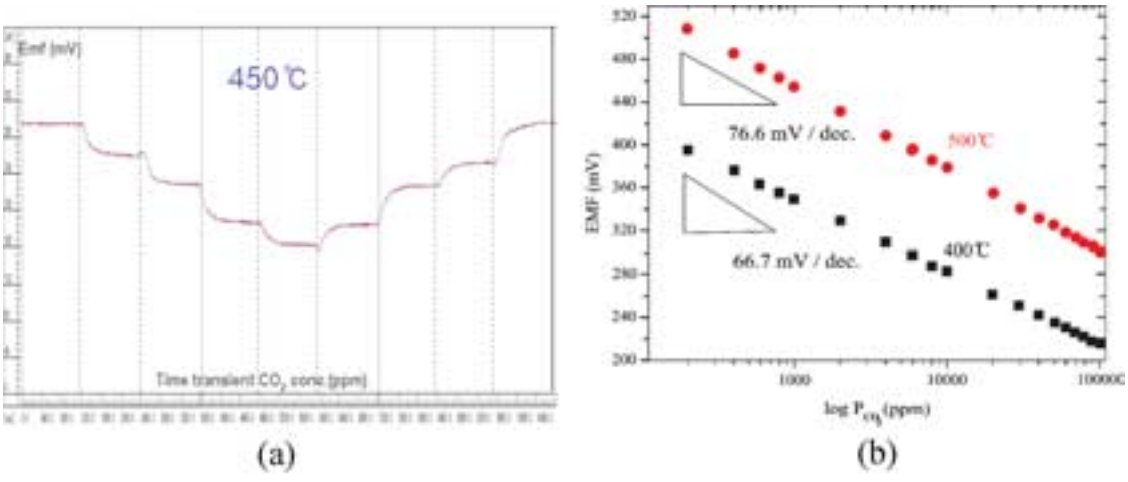

Figure 23 (a) The time response of the emf of the cell (114) and (b) emf vs. ln P_{CO_2} at 400°C and 500°C.

The chemical activity of Na_2O in NASICON [73] has been established as

$$\log a_{Na_2O} = -12050/T - 2.15 \qquad (110)$$

and the activity of Na_2O in β-alumina has been measured [66] using the following cell

$$Au, CO_2, O_2, Na_2CO_3|\beta - Al_2O_3|O_2, Au \qquad (111)$$

The overall reaction is $Na_2CO_3 = Na_2O + CO_2$ and the emf of the cell can be expressed as

$$E = -\left(\Delta G^{\circ}_{Na_2O} + \Delta G^{\circ}_{CO_2} - \Delta G^{\circ}_{Na_2CO_3}\right)/2F - (RT/2F)\ln\left[a_{Na_2O} P_{CO_2}\right] \qquad (112)$$

Hence, the activity of Na_2O can be obtained by measuring the cell emf for a given CO_2 partial pressure. Fig. 24 plots the activity of Na_2O for NASICON and β-alumina superimposed on the Na–C–O phase stability diagram.

According to Fig. 24, when β-alumina with a given activity of Na_2O is exposed to the CO_2-containing ambient, Na_2CO_3 can form and short-circuit the cell. Because NASICON has a lower Na_2O activity than β-alumina, it is more stable and subsequently has a wider detection range than β-alumina. In addition, NASICON shows good conductivity at a temperature as low as 600 K, whereas β-alumina cannot be used at lower than 700 K.

Unfortunately, NASICON and β-alumina can easily react with H_2S or SO_2 in the ambient to form sodium sulfate. Greater than 50 ppb SO_2 in the ambient could result in an irreversible breakdown of NASICON [67].

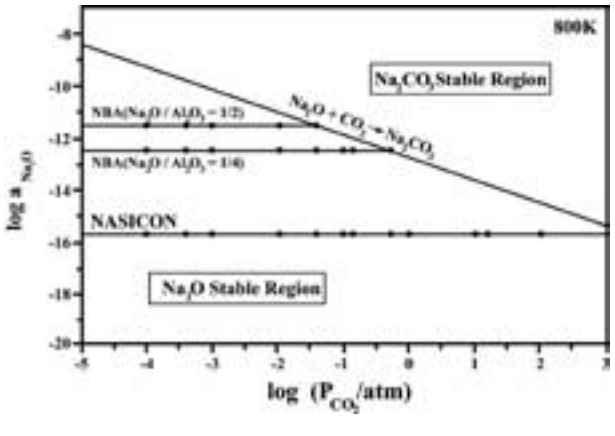

Figure 24 The stabilities of NASICON and β-alumina upon exposure to CO_2 gas at 800 K [66].

7.2.2. Sensing electrode

Sodium carbonate is generally used as the auxiliary phase with Au or Pt probes as the sensing electrode for a type III sensor involving a Na^+ ion conducting electrolyte. Many interference effects (or cross-sensitivity) can result from this auxiliary phase. For example, sodium sulfate is usually formed when carbonate is exposed to an ambient containing SO_2 or H_2S because of the negative standard Gibbs free energies for the reactions (113) and (114) [31, 64]:

$$Na_2CO_3 + SO_2 + 1/2O_2 = Na_2SO_4 + CO_2$$
$$\Delta G^{\circ} = -262.0\,\text{KJ}(500^{\circ}\text{C}) \qquad (113)$$

$$Na_2CO_3 + 2H_2S + 3/2O_2 = Na_2SO_4 + CH_4 + SO_2$$
$$\Delta G^{\circ} = -378.0\,\text{KJ}(500^{\circ}\text{C}) \qquad (114)$$

The presence of water vapor in the ambient is also reported to cause a strong interference with CO_2 detection; the response time increases and the emf values become far larger than those for dry CO_2. This degradation is believed to result from the reaction of the carbonate with water, producing hydrated compounds such as $NaHCO_3$ and NaOH. Miura [74] identified auxiliary phases with good water-resistance by mixing carbonates with low water solubility, such as $BaCO_3$, $CaCO_3$ and $SrCO_3$ with Na_2CO_3. Especially good performances were obtained for the hypereutectic composition of $BaCO_3$ and Na_2CO_3 (molar ratio of 1.7:1.0).

Though Li-electrolyte-based type III sensors show suppressed interference from humidity, the response

tends to deviate from the Nernstian behavior. Two possible reasons can cause this deviation: mixed (ionic and electronic) conduction in the electrolyte and the effect of a non-reversible electrode. The effect of mixed conduction on the CO_2 sensor was discussed in a recent publication [70]. A reversible electrode is necessary for maintaining thermodynamic equilibrium in an electrochemical sensor. A non-reversible electrode can induce polarization at the interface between the electrolyte and the electrode causing the potential to deviate from the equilibrium value.

7.3. Hydrogen sensor

In certain crystalline compounds, the proton moves by either a free proton mechanism (via H^+) or by a vehicle mechanism via species such as OH^-, H_3O^+ and NH_4^+. The former is mostly found in solids whereas the latter occurs in aqueous solutions. However, materials with wide open or layered structures such as SiO_2 and β-Al_2O_3, respectively, exhibit the vehicle mechanism to allow the passage of large molecular ions, such as H_3O^+ transport in β-Al_2O_3.

When oxides, especially perovskite-type oxides are exposed to environments containing water vapor or hydrogen gas, hydrogen dissolves into the oxides up to a few mol% or more to form proton defects as shown in Table III. These are stable protons at high temperature and their mobilities are higher than those of the oxygen ion and holes, which enables protonic conduction to occur. For example, the activation energy for the proton conduction, $Q_{OH_O^\bullet} \approx 0.74$ eV while $Q_{h^\bullet} \approx 1.21$ eV and $Q_{V_O^{\bullet\bullet}} \approx 2.5$ eV [75].

Typical perovskite oxides having the ABO_3 structure of Fig. 25 are cerates, titanates and zirconates, where aliovalent cation solutes such as Y^{+3}, Yb^{+3}, In^{+3}, Gd^{+3} or Nd^{+3} are doped at the B site to increase the conductivity. In general, cerates show higher conductivities than zirconates as shown in Fig. 26. However, their low chemical stability and mechanical strength make them unfavorable for practical applications. The zirconates with Ca, Ba and Sr in the A site are most widely used as proton conductors. When the dopants listed in Table IV are substituted on the Zr site, these materials exhibit proton conduction in H_2/O_2 ambient at temperatures from 600°C to 1000°C.

TABLE III The amount of hydrogen dissolved in various perovskite oxides per unit cell structure of ABO_3 [76]

Materials	Hydrogen equivalent per unit cell
$Ba_3Ca_{1.18}Nb_{1.82}O_{8.73}$ (BCN18)	0.18
$Ba_2YSnO_{5.5}$	0.5
$Ba_2InSnO_{5.5}$	0.5
$Ba_2In_2O_5$	1

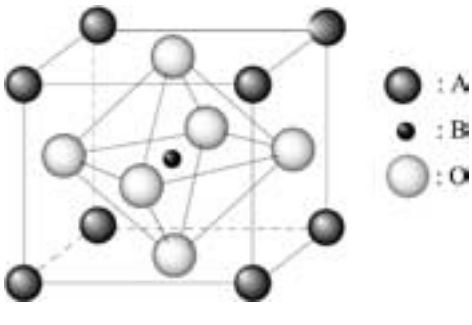

Figure 25 Unit cell of the perovskite structure.

TABLE IV Impurities doped in various zirconates [77, 78].

Zirconate oxides	Dopants
$CaZrO_3$	Al, Ga, In, Sc
$SrZrO_3$	Al, Ga, In, Y, Yb
$BaZrO_3$	Ga, In, Nd, Y, Dy

The proton-conducting properties of perovskite-type oxides were systematically investigated by Takahashi and Iwahara [79] in 1980. Their low proton conductivity makes them unsuitable for the use in fuel cells or amperometric devices. However, In-doped $CaZrO_3$ has been successfully developed as a commercial hydrogen probe for the detection of hydrogen dissolved in molten Al.

Since protons have a small ionic radius close to a bare nucleus, they cannot occupy a lattice or normal interstitial site in oxides but are always embedded in the electron cloud of an oxygen ion, forming a hydroxide defect, $OH_O^\bullet$. In the presence of water vapor, the dissolution of protons occurs through the reaction

$$H_2O(g) + V_O^{\bullet\bullet} + O_O^\times = 2OH_O^\bullet \qquad (115)$$

which, in terms of gas phase dissociation reaction $H_2O = H_2 + 1/2O_2$, can be divided into two separate partial reactions: the formation of ① the oxide and ② two hydroxide defects written as

$$\frac{1}{2}O_2 + V_O^{\bullet\bullet} + = O_O^\times + 2h^\bullet \qquad (116)$$

and

$$H_2(g) + 2O_O^\times + 2h^\bullet = 2OH_O^\bullet \qquad (117)$$

where electron and hole concentrations are connected via the intrinsic equilibrium for electronic defects.

$$e' + h^\bullet = 0 \qquad (118)$$

The formation of proton defects in oxides is affected by the Gibbs free energies of reactions (116) and (117), i.e., $\Delta G_{115} = \Delta G_{116} + \Delta G_{117}$. The reaction (116) would be favored for the oxides with a large negative value of Gibbs formation energy for oxygen vacancies (stable oxide) and with a large concentration of oxygen ion vacancies. Reaction (117) is favored for an oxide with higher basicity. The reaction entropies for reactions (116) and (117) are expected to have negative values due to the annihilation of gas molecules, which from the relation $\Delta G = \Delta H - T\Delta S$, indicates that the reactions shift to the left with increasing temperature. Therefore, one can expect a shift in the

concentration of positively charged defects in the order of $OH_O^{\bullet} \rightarrow h^{\bullet} \rightarrow V_O^{\bullet\bullet}$ as the temperature increases [81].

When aliovalent acceptor impurities are doped into the B site, the charge neutrality condition becomes

$$[M'_B] + [e'] = [OH_O^{\bullet}] + [h^{\bullet}] + 2[V_O^{\bullet\bullet}] \quad (119)$$

Therefore, the concentration of the proton solute increases in the oxides, in competition with other positively charged defects such as oxygen vacancies and holes.

From the known thermodynamic properties of Equations 116–118 and relation (119), the concentrations of four defects ($OH_O^{\bullet}$, $V_O^{\bullet\bullet}$, $h^{\bullet}$, e') can be calculated as a function of p_{H_2} and P_{O_2} for a constant concentration of acceptor dopant. For example, the map for the conduction domain in Fig. 27 can be drawn at a given temperature for In-doped $CaZrO_3$ where the equilibrium constants

$$K_{116} = [h^{\bullet}]^2/[V_O^{\bullet\bullet}]p_{O_2}^{1/2} \quad (120)$$

$$K_{117} = [OH_O^{\bullet}]^2/[h^{\bullet}]^2 p_{H_2} \quad (121)$$

$$K_{118} = [h^{\bullet}][e'] \quad (122)$$

and the electro-neutrality condition

$$2[V_O^{\bullet\bullet}] + [OH^{\bullet}] + [h^{\bullet}] = [In'_{Zr}] + [e'] \quad (123)$$

have been used.

Proton conduction becomes dominant over oxygen ion conduction for a wide range of oxygen and hydrogen activities at temperatures between 600°C to 800°C, where the monitoring of dissolved hydrogen content in an Al melt is performed.

The hydrogen dissolved in Al melt is measured by a potentiometric Galvanic cell with a proton-conducting electrolyte

$$(I)Pt,\ p'_{H_2}|H^+|p''_{H_2},\ Pt(II) \quad (124)$$

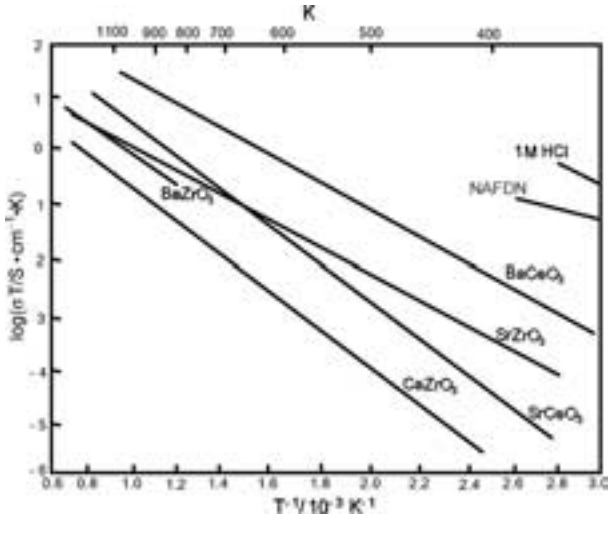

Figure 26 Proton-conductivities of various perovskite oxides [80].

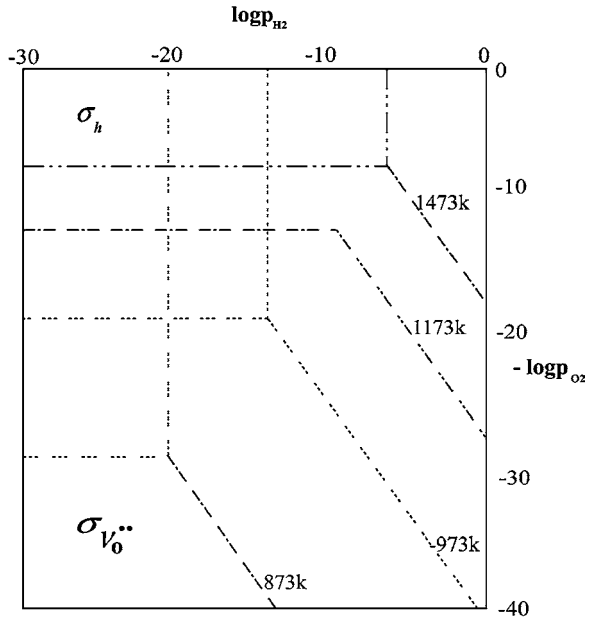

Figure 27 Conduction domains of various defects in In_2O_3-doped $CaZrO_3$ [75].

The voltage of the cell (124) can be written as

$$E = -\frac{RT}{2F} \ln \frac{p''_{H_2}}{p'_{H_2}} \quad (125)$$

where p''_{H_2} corresponds to the reference gas containing a known concentration of hydrogen gas, commercially 1% H_2-Ar. In practice, dissolution of hydrogen occurs by the reaction of water molecules in the gas phase,

$$3H_2O + 2Al \rightarrow 6H(inAl) + Al_2O_3 \quad (126)$$

where Sieverts' law, $S = kp_{H_2}^{1/2}$ is obeyed. Hence, the solubility of hydrogen in pure liquid Al is given by [82, 83]

$$\log S(\text{ml, STP}/100g\text{Al}) = 1/2 \log p_{H_2}(\text{atm}) - 2{,}760/T + 2.796 \quad (127)$$

or, in weight percent,

$$\log(\%H)_{Al} = 1/2 \log p_{H_2}(\text{atm}) - 2{,}760/T - 1.25 \quad (128)$$

Combining Equations 125 and 127 gives the amount of dissolved hydrogen in liquid Al as a function of voltage measured from the cell (124) at a given temperature.

$$\log S = 1/2 \log p_{H_2} + 5{,}039.798E/T - 2{,}760/T + 2.796 \quad (129)$$

A solid mixture such as TiH_2/Ti can be used to fix the hydrogen partial pressure in the reference electrode. In this case, the hydrogen activity is determined by the equilibrium

$$Ti(s) + H_2(g) = TiH_2(s) \quad (130)$$

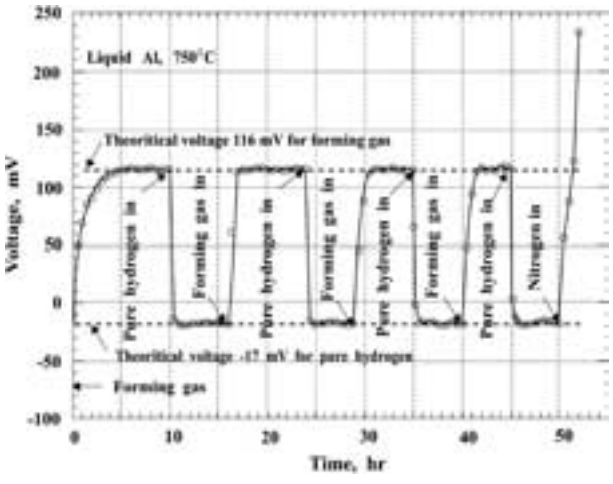

Figure 28 The voltage measured for H-containing pure Al melt at 750°C [84].

to give a fixed hydrogen pressure for p''_{H_2}

$$p_{H_2}(\text{atm}) = \exp(-17{,}734.68/T + 16.94) \quad (131)$$

Combining Equation 125, 128 and 131 gives the weight percent of dissolved hydrogen in Al as a function of the voltage

$$\log(\%\text{H})_{\text{Al}} = -6{,}610.5/T - 5{,}037E/T + 2.43 \quad (132)$$

Fig. 28 shows the measurement results obtained from a pure Al melt at 750°C, during which the gas atmosphere over the melt was cycled between pure hydrogen and forming gas ($N_2 + H_2$).

Acknowledgements

Technical comments by Mr. Chong-hoon Lee are greatly appreciated.

References

1. C. WAGNER, *Naturwissenschaften* **31** (1943) 265.
2. G. SCATCHARD, *J. Amer. Chem. Soc*. **75** (1953) 2883.
3. R. A. RAPP and D. A. SHORES, "Techniques of Metal Research," Vol IV, part 2 (Interscience Publisher, 1970) p. 123.
4. F. A. KRÖGER, *J. Amer. Ceram. Soc*. **49**(4) (1966) 215.
5. J. W. PATTERSON, *J. Electrochem. Soc*. **118** (1971) 1033.
6. H. NÄFE, *Soid State Ionics* **113–115** (1998) 205.
7. C. WAGNER, in Proc. Intern. Comm. Electrochem. Therm. Kinetics (CITCE), 7th Meeting Lindau (1955) (Butterworth Scientific Publ., London, 1957).
8. O. TILLEMENT, *Solid State Ionics* **68** (1994) 9.
9. C. WAGNER, *Z. Phys. Chem*. B **21** (1933) 25.
10. F. O. KOENIG, *J. Phys. Chem*. **44** (1940) 101.
11. C. WAGNER, in "Advances in Electrochemistry and Electrochemical Engineering," edited by Paul Delahay (Interscience Publishers, New York, 1966) Vol. 4, p. 1.
12. R. W. URE, *J. Chem. Phys*. **26** (1957) 1363.
13. J. SHORT and R. ROY, *J. Phys. Chem*. **67** (1963) 1860.
14. R. TAYLOR and H. SCHMALZRIED, *ibid*. **68** (1964) 2444.
15. E. ZINTL and U. CROATTO, *Z. Anorg. Allgem. Chem*. **242** (1939) 79.
16. C. TUBANT, H. REINHOLD and G. LIEBOLD, *ibid*. **197** (1931) 225.
17. E. BARSIS and A. TAYOR, *J. Chem. Phys*. **45** (1966) 1154.
18. L. W. STROCK, *Z. Phys. Chem.* B **25** (1934) 441; B **31** (1936) 132.
19. C. WAGNER, *Z. Electrochem.* **60** (1956) 4; **63** (1959) 1027.
20. D. RALEIGH, *J. Phys. Chem. Solids*. **26** (1965) 329.
21. R. A. RAPP, "Thermodynamics of Nuclear Materials" (IAEA, Vienna, 1968) p. 559.
22. C. B. ALCOCK, "Electromotive Force Measurements in High Temperature Systems" (Inst. of Mining and Metallurgy Publications, London, 1968).
23. J. W. PATTERSON, E. C. BOGREN and R. A. RAPP, *J. Electrochem. Soc*. **114** (1967) 752.
24. K. O. HEVER, *ibid*. **115** (1968) 830.
25. Y. Y. YAO and J. T. KUMMER, *J. Inorg. Nucl. Chem.* **29** (1967) 2453.
26. J. B. GOODENOUGH, H. Y. P. HONG and J. A. KAFALAS, *Mater. Res. Bull*. **11** (1976) 203.
27. C. LEE, S. A. AKBAR and C. O. PARK, *Sensors and Actuators* B **80** (2001) 234.
28. H. AONO, E. SUGIMOTO, Y. SADAOKA, N. IMANAKA and G. Y. ADACHI, *Solid State Ionics* **40/41** (1990) 38.
29. T. HIBIO, K. MIZUTANI, T. YAMAJIMA and H. IWAHARA, *ibid*. **57** (1992) 303.
30. D. A. STEVENSON, N. JIANG, R. M BUCHANAN and F. E. G. HENN, *ibid*. **62** (1993) 279.
31. H. IWAHARA, T. YAMAJIMA, HIBINO, K. OZAKI and H. SUZUKI, *ibid*. **61** (1993) 65.
32. W. L. WORRELL and Q. G. LIU, *J. Electr. Chem. Interf. Electrochem*. **168** (1984) 355.
33. G. HOTZEL and W. WEPPNER, in Proc. 6th Riso-Intern. Sympo. On Transport-Structure Relations in Fast Ion and Mixed Conductor (Riso Natl. Lab., Roskilde, 1985) p. 401.
34. N. MIURA, S. YAO, Y. SHIMIZU and N. YAMAZOE, *Sensors and Actuators* B **13/14** (1993) 387.
35. P. T. MOSELY, *Meas. Sci. Technol*. **8** (1997) 223.
36. F. H. GARZON, R. MUKUNDAN and E. L. BROSKA, *Solid State Ionics* **136/137** (2000) 633.
37. T. H. ESTELL and S. N. FLENGAS, *J. Electrochem. Soc*. **118**(12) (1989) 1890.
38. C. N. SATTERFIELD, "Mass Transfer in Heterogeneous Catalysis" (MIT Press, Cambridge, 1970) p. 30.
39. J. O. HIRSCHFIELDER, C. F. CURTISS and R. B. BIRD, "Molecular Theory of Gases and Liquids" (Wiley Publ., New York, 1967) p. 14.
40. H. DIETZ, *Solid State Ionics* **6** (1982) 175.
41. R. JACKSON, "Transport in Porous Catalysts" (Elsevier, Amsterdam, 1977) p. 9.
42. T. USUI, Y. KURUMIYA, K. NURI and M. NAKAZAWA, *Sensors and Actuators* **16** (1989) 345.
43. T. USUI, A. ASADA, M. NAKAZAWA and H. OSANAI, *J. Electrochem. Soc*. **136**(2) (1989) 534.
44. Z. PENG, M. LIU, ED. BALKO, *Sensors and Actuators* B **72** (2001) 35.
45. H. SCHMALZRIED, *Z. Phys. Chem*. (Frankfurt) **38** (1963) 87.
46. *Idem*., *Z. Electrochem*. **66** (1962) 572.
47. W. WEPPNER,"Solid State Ionics," edited by M. Balkanski, T. Takahashi and H. L. Tuller (Elsevier Science Pub., 1992) p. 29.
48. A. MENNE and W. WEPPNER, in Proc. Third Int. Meeting on Chemical Sensors (Cleveland Ohio, 1990) p. 225.
49. K. NISHIO, "The Fundamentals of Automotive Engine Control Sensors" (Fontis Media, SA, 2001) p. 91.
50. F. MENIL, V. COILLARD and C. LUCAT, *Sensors and Actuators* B **67** (2000) 1.
51. K. SAJI, H. KONDO, T. TAKEUCHI and I. IGARASHI, *J. Electrochem. Soc*. **135**(7) (1988) 1686.
52. J. E. ANDERSON and Y. B. GRAVES, *ibid*. **128**(2) (1981) 294.
53. W. J. FLEMING, *ibid*. **124**(1) (1977) 21.
54. S. OH, *Sensors and Actuators* B **20** (1994) 33.
55. H. TANAKA, S. NISHIMURA, S. SUZUKI, M. MIKI, T. HARADA, M. KANAMARU, S. UENO and N. ICHIKAWA, SAE No. 890299 (1989).
56. B. K. KIM, J. H. LEE and H. KIM, *Solid State Ionics* **86–88** (1996) 1079.
57. W. C. VASSELL, E. M. LOGOTHESIS and R. E. HETRICK, SAE Paper No. 841250 (1984).
58. S. SOEJIMA and S. MASE, SAE Paper No. 850378 (1985).

59. T. SASAYAMA, T. YAMAUCHI, R. BYERS, S. SUZUKI and S. UENO, SAE Paper No. 910501 (1991).
60. A. D. COLVIN, J. S. RANKIN and K. R. CARDUNER, *Sensors and Actuators* B **12** (1993) 83.
61. M. GAUTHIER and A. CHAMBERLAND, *J. Electrochem. Soc*. **124** (1977) 1579.
62. R. COTE and C. W. BALE, *ibid*. **131** (1984) 63.
63. K. SINGH, P. AMBEKAR and S. S. BHOGA, *Solid State Ionics* **122** (1999) 191.
64. J. LIU and W. WEPPNER, in "Solid State Ionics," edited by M. Balkanski, T. Takahashi and H. L. Tuller (Elsevier Science Publishers B. V., 1992) p. 61.
65. M. HOLZINGER, J. MAIER and W. SITTE, *Solid State Ionics* **86–88** (1996) 1055.
66. T. MARUYAMA, S. SASAKI and Y. SAITO, *ibid*. **23** (1987) 107.
67. T. LANG, H.-D. WIEMHOFER and W. GÖPEL, *Sensors and Actuators* B **34** (1996) 383.
68. M. A-PORTA and R. V. KUMAR, *ibid*. **71** (2000) 173.
69. N. MIURA, S. YAO, Y. SHIMIZU and N. YAMAZOE, *ibid*. **9** (1992) 165.
70. C. O. PARK, C. LEE, S. A. AKBAR and J. HWANG, *ibid*. **88** (2003) 53.
71. G. ADACHI and N. IMANAKA, in Proc. Symp'on Chemical Sensors II, edited by M. Butler, N. Yamazoe and A. Ricco, J. Electrochem. Soc., Vol. 93, p. 182.
72. R. STEVENS and J. G. P. BINNER, *J. Mater. Sci*. **19** (1984) 695.
73. G. M. KALE and K. T. JACOB, *J. Mater. Res*. **4**(2) (1989) 417.
74. N. MIURA, S. YAO, Y. SHIMIZU and N. YAMAZOE, *Sensors and Actuators* B **9** (1992) 165.
75. N. KURITA, *J. Electrochem. Soc*. **142**(5) (1995) 1552.
76. T. NORBY, *Solid State Ionics* **125** (1999) 1.
77. H. IWAHARA, T. YAJIMA, T. HIBINO, K. OZAKI and H. SUZUKI, *ibid*. **61** (1993) 65.
78. R. SLADE, S. D. FLINT and N. SINGH, *ibid*. **82** (1995) 135.
79. T. TAKAHASHI and H. IWAHARA, *Rev. Chim. Miner*. **17** (1980) 243.
80. N. FUKATSU, *J. Alloys Comp.* **231** (1995) 706.
81. K. D. KREUER, *Solid State Ionics* **97** (1997) 1.
82. C. E. RANSLEY and H. NEUFELD, *J. Inst. Metals* **74** (1948) 599.
83. R. GEE and D. J. FRAY, *Metall. Trans*. B **9** (1978) 427.
84. Y. ZHANG and R. A. RAPP, The Ohio State University, Personal Communications.